1

2

Reversible lipid mediated pH-gating of connexin-46/50 by cryo-EM

4

Authors:

Joshua M. Jarodsky[1,2], Janette B. Myers[1,2,3] and Steve L. Reichow[1,2,3,*]

7

8

Affiliations:

[1] Department of Chemical Physiology and Biochemistry, Oregon Health and Science University, Portland, OR 97239, USA.

[2] Vollum Institute, Oregon Health and Science University, Portland, OR 97239, USA.

[3] Pacific Northwest Cryo-EM Center, Oregon Health and Science University, Portland, OR, 97201, USA.

14

* Correspondence: reichow@ohsu.edu

16

17

18

19

20

21

22

23

24

25

26

27

Keywords:

connexin, gap junction, cryo-EM, pH regulation, lipid gating, large-pore channel

30

31

32

33 **ABSTRACT**

34 Gap junctions, formed by connexin proteins, establish direct electrical and metabolic coupling between

35 cells, enabling coordinated tissue responses. These channels universally respond to intracellular pH

36 changes, closing under acidic conditions to limit the spread of cytotoxic signals during cellular stress,

37 such as ischemia. Using cryo-electron microscopy (cryo-EM), we uncover insights into the structural

38 mechanism of pH-gating in native lens connexin-46/50 (Cx46/50) gap junctions. Mild acidification drives

39 lipid infiltration into the channel pore, displacing the N-terminal (NT) domain and stabilizing pore closure.

40 Lipid involvement is both essential and fully reversible, with structural transitions involving an ensemble

41 of gated-states formed through non-cooperative NT domain movement as well as minor populations of a

42 distinct destabilized open-state. These findings provide molecular insights into pH-gating dynamics,

43 illustrating how structural changes may regulate gap junction function under cellular stress and linking

44 Cx46/50 dysregulation to age-related cataract formation.

45

46

47

48

49

50

51

52

53

54

55

56

57

58

59

60

61

62

63

64

65

66

67

68

69

INTRODUCTION

Connexins form intercellular channels, known as gap junctions, that enable direct cell-to-cell communication, allowing tissues to function as a syncytium by coordinating long-range electrical and metabolic activity[1,2]. These channels are critical in numerous physiological processes, and their dysfunction is linked to diverse diseases, including blindness, deafness, arrhythmia, stroke, neuropathy, skin disorders, and cancer[3-5].

In addition to propagating cellular signals, gap junctions play a vital role in cellular stress responses. They dilute cytotoxic signals (e.g., potassium buffering by glial cells), and may also uncouple damaged cells from healthy tissue, preventing bystander effects or the so-called "kiss of death"[6,7]. Uncoupling is triggered by stress-induced gating mechanisms sensitive to transjunctional voltage and cytosolic chemical signals, like H^+ and Ca^{2+} [8-14]. Intracellular acidification, a hallmark of ischemia and cataract, is a universal regulator of gap junctional gating[15-18]. However, despite recent advances[19], the molecular mechanisms underpinning pH-induced gating remain poorly defined.

Structurally, gap junctions are composed of twelve connexin subunits, forming either homomeric or heteromeric/heterotypic assemblies depending on isoform composition (21 isoforms in humans)[20,21]. Each hemichannel, formed by six connexins, docks with its counterpart in an adjacent cell to create a large-pore intercellular channel (~1 kDa cutoff) capable of passaging ions, metabolites, and signaling molecules[22]. Each connexin subunit consists of four transmembrane helices (TM1–4), two extracellular loops (EC1–2) involved in junction formation, and an N-terminal domain (NT) implicated in channel selectivity and gating[23-26] (see Fig. 1a). Intracellular loop (ICL) and C-terminal (CT) regions involved in trafficking and regulation are largely disordered and highly variable among isoforms[20,21].

Early models of pH-gating based on studies of Cx43 and Cx50 proposed a "ball-and-chain" mechanism, linking the CT in pore occlusion[27-31]. However, subsequent studies have shown that pH gating in several isoforms, including Cx46 and Cx50, does not require the CT[32-35]. More recently, the NT domain has been implicated as a pH-gating particle, supported by cryo-electron microscopy (cryo-EM) studies of Cx26[19]. Though limited resolution of this study precluded atomic-level details of the gating mechanism, the study describes pH-induced conformational changes in the NT that result in pore occlusion. The NT's involvement in pH-gating aligns with its conserved nature and its suggested role in other gating mechanisms, such as "fast" voltage-gating, underscoring its central function in connexin regulation[23,25,26,36-38].

Recent cryo-EM studies of various connexin isoforms have revealed diverse NT conformations influenced by environmental conditions and suggest a potential role for lipids in modulating NT conformational states (recently reviewed[39]). However, the origination of pore-bound lipids in these studies remains unclear, as

3

107   hydrophobic molecules can diffuse into the large-pore of these channels during detergent extraction or

108   reconstitution into lipid nanodiscs, complicating interpretation of their potential functional relevance.

109

110   Here, using single-particle cryo-EM, we investigated the pH-gating mechanism of native Cx46/50

111   channels from aged lens tissue. We show that at neutral pH, channels predominantly adopt a stabilized

112   open-state devoid of pore-bound lipids, consistent with prior studies[40,41]. When this sample is exchanged

113   to mildly acidic conditions known to gate these channels in electrophysiology studies[32-35], structural

114   changes induce lipid infiltration into the pore, displacing the NT and driving an ensemble of gated states.

115   Lipid infiltration is shown to originate from the surrounding lipid environment, to be essential for gating,

116   fully reversible upon return to neutral pH, and is proposed to be linked to protonation of conserved

117   histidines. Structural deconvolution reveals non-cooperative NT movements contributing to multiple

118   gated states, alongside minor populations of stabilized and destabilized open-states. Collectively, these

119   findings provide critical insights into the dynamic interplay between lipids and pH-gating in Cx46/50,

120   offering molecular insights into age-related cataract formation and establishing a framework for

121   understanding connexin regulation under cellular stress.

122

123   **RESULTS**

124   *Low pH gated-state of connexin-46/50*

125   Native Cx46/50 channels were purified from aged ovine lens tissue, containing native C-terminal

126   truncations[42,43], and reconstituted into MSP1E1 nanodiscs containing dimyristoyl-phosphatidylcholine

127   (DMPC) lipids at pH 7.4, as previously described[41]. The reconstituted channels were then buffer-

128   exchanged to pH 5.8 via gel filtration, to mimic low-pH conditions shown to gate C-terminal truncation

129   variants of Cx46 and Cx50 channels in cellular functional studies[32-35] (Extended Data Fig. 1,2). Cryo-EM

130   single-particle analysis resolved a low-pH gated-state structure of Cx46/50 at 2.2 Å global resolution (Fig.

131   1b; Extended Data Fig. 3,4 and Table 1; Collection #1).

132

133   Heteromeric/-typic assembly patterns of Cx46/50 were indistinguishable from the cryo-EM density,

134   consistent with prior studies[40,41] and the >80% sequence identity across structured regions of the two

135   isoforms. Atomic models for both isoforms were refined into a D6-symmetrized map, encompassing TM1-

136   4, EC1-2, and the NT gating domain, while the CT and ICL regions remained largely unresolved due to

137   intrinsic disorder (Fig. 1c; Extended Data Fig. 5 and Table 1). Over 400 lipids and 900 water molecules

138   were also resolved, with extracellular leaflet lipids exhibiting long-range hexagonal packing, consistent

139   with previous observations[41]. Given the similarity between Cx46 and Cx50, Cx46 is presented as the

140   archetype, with isoform-specific differences noted where relevant (Extended Data Fig. 6).

141

142   The pH gated-state is characterized by inward displacement of the NT domain, as compared to the

143   stabilized open-sate at neutral pH[41], shifting 20° toward the pore center (Cα r.m.s.d. = 5.5 Å over the NT

144 domains) (Fig. 1a,d,e; Extended Data Fig. 6). While the local resolution limited modeling of the NT to

145 residue W4, a plug-like density at the center of the pore suggests full occlusion by proximal residues G2

146 and D3 (not explicitly modeled), consistent with complete channel closure (Fig. 1b inset,g,h). An

147 additional constriction site at S5 narrows the pore in this region to 7.5 Å (compared to 11.6 Å in the open-

148 state at D3), further illustrating the alteration of the NT in the pH-gated state (Fig. 1i).

149

150 The low pH gated-state of the NT is supported by infiltrated lipids, disrupting hydrophobic NT-TM1/2

151 interactions that anchor the NT in the stabilized open-state (Fig. 1a,c,g). The infiltrated lipids occupy a

152 hydrophobic pocket formed by TM1/2 within the channel lumen, intercalated beneath the NT and

153 stabilizing its displacement in the gated conformation. This gated-state appears further stabilized through

154 a network of inter-subunit electrostatic interactions. Specifically, the S5 hydroxyl group forms a hydrogen

155 bond with the backbone of F6 on a neighboring NT, while the E12 carboxylate forms a salt-bridge with

156 R9 (N9 in Cx50) (Fig. 1h).

157

158 NT movement is coupled with a global clockwise rearrangement of the transmembrane helices, as viewed

159 from the cytoplasmic side, that reinforce the gated NT conformation (Fig. 1d,e). TM2 exhibits the largest

160 displacement, facilitated by a conserved proline kink at P88 that shifts the cytoplasmic portion of TM2 by

161 ~8° toward the pore, enabling hydrophobic interactions between L93 (V93 in Cx50) on TM2 and A14

162 (V14 in Cx50) on the NT (Fig. 1e). Additionally, subtle structural variation is observed compared to the

163 open-state in the π-helix region of TM1 (residues ~39–41) that forms a kink separating the para-helical

164 region leading to EC1 (Extended Data Fig. 6).

165

166 *Lipid stabilization of the low pH gated-state*

167 Beyond NT movement, the most striking difference between the open and gated-states is lipid

168 translocation into the pore and at inter-subunit interfaces (Fig. 1c; Fig. 2). Two pore-bound lipids (PL1,

169 PL2) form a double-layer hydrophobic "gasket" stabilizing the NT domain in the gated-state, while an

170 interstitial lipid (IL) is identified intercalated at the subunit interface (Fig. 2a,b).

171

172 PL1, modeled as a nine-carbon acyl chain of DMPC, occupies a hydrophobic groove formed by TM1/2

173 of one subunit and TM1 of a neighboring subunit, displacing NT hydrophobic residues (W4, L7, and L11)

174 that occupy this site in the open-state (Fig. 2c,d). The cytoplasmic portion of TM2 shifts toward the center

175 of the pore under low-pH conditions, bringing L93 (V93 in Cx50) on TM2 ~2.8 Å closer to L26 on TM1,

176 contributing to NT displacement (Fig. 2c,d).

177

178 PL2 is positioned atop PL1 and forms additional interactions with TM1 of an adjacent subunit (Fig. 2a).

179 Although the complete phosphocholine (PC) headgroup of PL2 could not be confidently modeled, the

180 weak features extending from the U-shaped density suggest the headgroup extends toward the solvent,

5

181 with the acyl chains oriented toward the hydrophobic pocket formed by PL1, TM1, and the NT (Fig. 2e,f).
182 The hydrophobic anchoring residues of the NT rest on PL2, with the indole nitrogen of W4 positioned
183 near the ester backbone of this lipid, potentially contributing to the stability of binding at this site (Fig.
184 2e,f).

185

186 The IL intercalated at the subunit interfaces aligns with the intercellular leaflet (Fig. 2a,b). The IL exhibits
187 splayed acyl chains, with one chain forming extensive hydrophobic contacts with TM1/4 and TM2 of
188 adjacent subunits and the other chain penetrating toward the NT and interacting with Q15 (N15 in Cx50)
189 (Fig. 2g,h). These extensive interactions, particularly with TM2 and the NT, likely contribute to stabilizing
190 the gated-state conformation. Notably, the IL density is absent in the open-state structure, suggesting a
191 pH-dependent interaction and potential entry/exit site for lipid infiltration into the pore (discussed below).

192

193 *pH-gating is lipid dependent and reversible*
194 We next sought to demonstrate that a lipid environment is required for pH-gating of Cx46/50 and that
195 lipid recruitment into the pore is a reversible process driven by pH conditions. First, to determine lipid
196 dependence, Cx46/50 channels were reconstituted into amphipol (PMAL-C8) at pH 7.4, following
197 established methods for obtaining the open-state structure[40], and then buffer-exchanged to pH 5.8. Cryo-
198 EM single-particle analysis resulted in a 2.7 Å reconstruction, with NT domains resolved adopting the
199 stabilized open-state conformation (Cα r.m.s.d. = 0.2 Å)[41], with no lipids or detergent in the pore (Fig. 3a;
200 Extended Data Fig. 2,6,7 and Table 1; Collection 2), confirming lipid dependence of the pH-gated state.

201

202 Next, to ensure lipids enter the pore as a result of low pH-induced structural changes, rather than by
203 nanodisc reconstitution artifacts, the following control experiments were conducted. Cx46/50 channels
204 reconstituted into nanodiscs at pH 7.4 were divided into two samples and buffer-exchanged to either
205 neutral (pH 7.4 control) or low pH (pH 5.8) conditions (Extended Data Fig. 2; Collections 3 and 4,
206 respectively). Cryo-EM 3D reconstruction of the neutral pH sample yielded a 2.0 Å map with NT domains
207 in the stabilized open-state and a pore free of lipids or detergent (Fig. 3b; Extended Data Fig. 8). In
208 contrast, the low pH sample produced a 2.6 Å map, revealing PL lipids stabilizing the NT in the gated-
209 state (Fig. 3c and *inset*), confirming that lipids are translocated from the local lipid environment in
210 response to low pH-induced structural changes.

211

212 Finally, reversibility of lipid-mediated gating was tested by returning the low pH-gated channels to neutral
213 pH conditions. Here, Cx46/50 channels reconstituted into nanodiscs at pH 7.4 were buffer-exchanged to
214 pH 5.8 to induce the gated-state. This sample was then split into two groups: one remained at pH 5.8
215 during buffer exchange (pH 5.8 control), and the other was dialyzed back to pH 7.4 (reversed pH 7.4)
216 (Extended Data Fig. 2; Collections #5 and #6, respectively). Cryo-EM reconstruction of the pH 5.8 control
217 yielded a 2.3 Å map, confirming the NT gated-state with PL lipids (Fig. 3d and *inset*; Extended Data Fig.

218   9). In contrast, reconstruction of the reversed pH 7.4 sample produced a 2.0 Å map, showing the

219   stabilized open-state conformation devoid of pore-bound lipids (Fig. 3e). These findings confirm that lipid

220   translocation is reversible and essential for pH-dependent gating observed by cryo-EM.

221

222   *Putative role of conserved histidine pH-sensors*

223   Having established pH gating is lipid-mediated, we next examined the potential mechanism underlying

224   H⁺-induced conformational changes. Conserved histidine residues have been suggested to play a key

225   role in the pH-dependent gating of several connexins[33,44-46]. These cytosolic sites correspond to H17 and

226   H95 in Cx46/50 (Extended Data Fig. 6). The role of conserved histidine residues in pH gating are

227   consistent with experimentally derived gating response pKa values of C-terminally truncated Cx46/50

228   (pKa ~6.6 for Cx46[34] and ~7.1 for Cx50[32]) and the universal nature of pH sensing across connexin

229   isoforms.

230

231   A mechanistic role for H95 in pH sensing had not been previously apparent, as it is positioned on TM2

232   facing the lipid environment. In the pH-gated state of Cx46/50, the imidazole ring of H95 lies within 3.0 Å

233   of the negatively charged phosphate headgroup of the interstitial lipid (IL) (Fig. 4a). This proximity

234   suggests that protonated H95 forms a salt-bridge with the IL, stabilizing the gated NT/TM2 conformation.

235   Coulombic surface potential analysis shows a dramatic shift to positive potential at this binding site under

236   acidic conditions (Fig. 4b,c). At neutral pH, deprotonation of H95 would disrupt this interaction (Fig. 4c),

237   consistent with the absence of lipid density at this site in the open-state structures. These findings

238   implicate H95 in recruiting the IL to its binding site and in stabilizing the gated state in a pH-dependent

239   manner.

240

241   Notably, mutating the equivalent H95 site does not eliminate pH sensitivity in Cx43[46] or Cx46[33], indicating

242   additional pH-sensing residues contribute to gating. H17, another highly conserved histidine, has also

243   been implicated as a pH-sensor in functional studies of Cx26[44] and Cx36[45]. H17 resides at the NT-TM1

244   hinge near the channel entrance, at a similar z-position to H95 relative to the pore axis (Fig. 4a). At neutral

245   pH, H17 interacts with V96 (A96 in Cx50) and L97 (V97 in Cx50) on TM2 (Fig. 4d,e). Under acidic

246   conditions, these contacts are maintained, while correlated rearrangements of the NT and TM2 position

247   the protonated sidechain of H17 within 3.4 Å of the negatively charged carboxylate group on E16,

248   enabling formation of a salt-bridge (Fig. 4d,f). This stabilizing interaction may also contribute to reinforcing

249   the NT gated conformation.

250

251   *Low pH induces an ensemble of gated- and open-states*

252   Single-channel recordings show acidic conditions induce a complex "slow" gating transition, with

253   channels fluctuating between closed and open states[33,47]. In contrast, at neutral pH and minimal

254   transjunctional voltage, Cx46 and Cx50 channels predominantly adopt an open-state[26,31,48-50]. In

7

255 agreement with this behavior, our structural analysis revealed pronounced conformational heterogeneity

256 induced by low pH conditions, particularly within the NT.

257

258 To investigate the structural basis of this heterogeneity, and its potential relationship to the dynamic

259 gating behavior, cryo-EM datasets for Cx46/50 at low pH were analyzed using 3D variability analysis

260 (3DVA)[51] (Fig. 5). The primary principal component revealed NT domains sampling both open and gated

261 conformations symmetrically across the channel, accompanied by conformational changes in TM2

262 (Supplemental Movie 1), consistent with the structural rearrangements described above.

263

264 Particles corresponding to distinct states along the principal component were pooled for 3D

265 reconstruction and used to estimate state distributions (Fig. 5a; see Methods). Across all low-pH datasets

266 (Collections #1, #4, and #5), 43.2% ± 2.3% of particles were resolved in the lipid-mediated gated-state,

267 while 18.2% ± 5.3% represented the open-state (mean ± s.e.m.; n = 3) (Fig. 5b). Notably, the open-state

268 resolved at low pH was nearly identical to the stabilized open-state at pH 7.4 (Cα r.m.s.d. = 0.2 Å;

269 Extended Data Fig. 6) and lacked pore-bound lipids.

270

271 In addition to the stabilized open and gated-states, a third state, termed the "destabilized open-state,"

272 was also identified along the same principal component, accounting for 38.5% ± 6.8% of low-pH particles

273 (n = 3) (Fig. 5a,b). An atomic model built into a 3D reconstruction resolved to 2.2 Å (from Collection #1)

274 showed the destabilized open-state resembles the stabilized open-state (Cα r.m.s.d. = 0.7 Å; Extended

275 Data Fig. 6), but with subtle distinguishing differences in the NT and TM2 domains, as well as in the

276 hydrogen bond patterns defining the TM1 π-helix kink at residues ~39–41 (Fig. 5c; Extended Data Fig.

277 4-6).

278

279 In the destabilized open-state, the NT remains anchored to the lumen by hydrophobic residues (W4, L7,

280 and L11) but adopts a distinct conformation, with a local Cα r.m.s.d. of 1.9 Å relative to the stabilized

281 open-state NT. TM2 shifts ~1.6 Å toward the pore center and bends by ~6.4°, resembling but less

282 pronounced than the movements of the gated-state (Fig. 5c). This conformation introduces a new pore-

283 constriction site at S5, reducing the pore diameter to 9.7 Å in Cx46, which is narrower than the stabilized

284 open-state (11.6 Å) but still sufficient for permeation of hydrated ions.

285

286 *Rare states detected at neutral pH*

287 Previously, under neutral pH cryo-EM conditions, we have only detected the stabilized open-state of

288 Cx46/50[40,41]. Consistent with this, 3DVA performed on neutral pH nanodisc datasets (Collections #3 and

289 #6), as well as the amphipol low-pH dataset (Collection #2), revealed minimal NT heterogeneity, with

290 variability limited to a slight "wobble" of TM2 (Supplemental Movie #). However, this approach may have

291 lacked the sensitivity to detect rare conformational states within the dataset. Therefore, as an approach

292   to enhance detection, we combined low-pH and neutral pH nanodisc datasets (Collections #3, #4 and

293   #5, #6), ensuring a substantial representation of each state, and reanalyzed the combined particle set

294   using 3DVA. This approach successfully resolved all three states (stabilized open, destabilized open,

295   and gated) allowing for their classification and independent reconstruction from particles belonging only

296   to the neutral pH dataset (Fig. 5a; see Methods).

297

298   This analysis further details the differences in state distributions between neutral and low pH datasets.

299   At neutral pH, 87.0% ± 9.5% of particles were in the stabilized open-state, 10.7% ± 8.1% in the

300   destabilized open-state, and only 2.4% ± 1.4% in the lipid-mediated gated-state (n = 2) (Fig. 5a,b). In the

301   sample that was never exposed to low pH (Collection #3), the stabilized open-state accounted for 96.4%

302   of particles, with the destabilized open-state and lipid-mediated gated-state representing 2.6% and 1.0%,

303   respectively (Fig. 5a,b; Extended Data Fig. 8).

304

305   The distribution of open-state channels at neutral pH closely aligns with single-channel electrophysiology

306   studies conducted under minimal transjunctional voltage[26,31,48-50], underscoring the agreement between

307   structural and functional analyses. In contrast, the observed proportion of low pH gated-state channels

308   deviates from expectations from electrophysiology studies, which would predict a predominance of closed

309   channels at the low pH conditions used for cryo-EM[32-35]. These discrepancies may stem from the absence

310   of transjunctional voltage in cryo-EM conditions, as well as other methodological differences.

311   Alternatively, they may indicate additional underlying heterogeneity in pH-gating transitions that was not

312   fully captured by this approach (see below).

313

314   *Non-cooperative gating of the NT-domain*

315   In addition to symmetric gating movements of the NT on both sides of the Cx46/50 intercellular channel,

316   3DVA of the low-pH datasets also revealed asymmetric gating movements of the NT domain, with each

317   hemichannel operating independently (Collections #4 and #5) (Fig. 6a; Supplemental Movie 1). To further

318   deconvolute the gated-state heterogeneity and to investigate potential cooperativity within hemichannels,

319   cryo-EM density for individual subunits were isolated using symmetry expansion and signal subtraction,

320   followed by 3D classification on the individual subunits. This approach distinguished subunits in the gated

321   and open-states based on NT characteristics, though differences between stabilized and destabilized

322   open-states could not be resolved (Fig. 6b; Extended Data Fig. 3,8,9). Among signal-subtracted subunits

323   from low pH datasets, 67.0% ± 0.5% (mean ± s.e.m.; n = 3; Collections #1, #4 and #5) were identified in

324   the gated-state. In contrast, the same workflow applied to neutral pH datasets (Collections #3 and #6)

325   exclusively identified subunits in the open-state conformation (Extended Data Fig. 8,9).

326

327   To quantify the frequency of open and gated-state monomers within parent gap junction particles,

328   metadata from the symmetry expansion protocol were analyzed (see Methods). Remarkably, fully gated-

9

329   states were rare, comprising only 1.7% ± 0.2% of gap junction particles and 14.4% ± 0.6% at the

330   hemichannel level (mean ± s.e.m.; n = 3) (Fig. 6c,d). Subunit distributions in the gated-state followed a

331   Boltzmann-like pattern, with nine gated subunits being the most frequent configuration (23.4% ± 0.3%; n

332   = 3) (Fig. 6c). A similar trend was observed at the hemichannel level, with five gated subunits being most

333   prevalent (33.3% ± 0.5%; n = 3) (Fig. 6d). States containing two to four gated subunits per hemichannel

334   were observed in multiple configurations, and their populations closely matched predicted values for

335   random distribution (Fig. 6e).

336

337   Notably, no fully open-state channels were observed under low-pH conditions, and < 0.5% were identified

338   with 1–3 gated protomers. These findings suggest that NT pH-gating occurs independently between

339   neighboring monomers under cryo-EM conditions, supporting a non-cooperative gating mechanism.

340   Moreover, the prevalence of subunits adopting a gated conformation under acidic conditions more closely

341   aligns with functional results, particularly considering models that suggest just a single subunit may be

342   sufficient to initiate gating of gap junction channels[36] (see Discussion).

343

344   *Comparison to other connexin structures*

345   The pH-gated structure of Cx46/50 shares similarities as well notable differences with previously reported

346   gap junction structures obtained under chemical gating conditions, such as Cx26 at pH 6.4[19], Cx26

347   treated with CO_2 maintained at pH 7.4[52] and Cx43 at pH 8.0[53]. The TM and EC domains of Cx46/50 align

348   closely with these structures, with Cα r.m.s.d. values (excluding the NT and cytoplasmic portion of TM2)

349   ranging from 0.6–0.8 Å. In contrast, significant variations in NT conformations are evident across these

350   structures; yet, the NT consistently contributes to the formation of the primary constriction site of the

351   channel (Fig. 7a,b).

352

353   Among the compared structures, the NT of Cx26 treated with CO_2 at pH 7.4 is most similar to the pH-

354   gated NT of Cx46/50 (Cα r.m.s.d. = 1.2 Å). In contrast, the largest deviation is observed in Cx43 (Cα

355   r.m.s.d. = 12.2 Å), where the NT adopts a near-parallel orientation relative to the membrane bilayer.

356   Interestingly, the NT of Cx46/50 shows substantial deviations with the pH-gated Cx26 structure (Cα

357   r.m.s.d. = 9.1 Å), although their proximal positions indicate a shared role in pH gating (Fig. 7a,b).

358   However, some discrepancy between these studies may reflect the limited resolution of the cryo-EM

359   density used for modeling the Cx26 pH-gated state[19].

360

361   Correlated with NT displacement, distinct conformational changes in TM2 were also observed. Compared

362   to the stabilized open-state of Cx46/50, all other models display a more bent conformation localized to

363   the cytoplasmic region of TM2 beyond the conserved proline kink (P88 in Cx46/50; P87 in Cx26 and

364   Cx43) (Fig. 7a). When compared to this region of TM2 in the pH-gated state of Cx46/50, Cx43 at pH 8.0

365   showed the smallest deviation (Cα r.m.s.d. = 1.2 Å), followed by Cx26 treated with CO_2 (Cα r.m.s.d. =

366   2.2 Å), while Cx26 at low pH exhibited the largest deviation (Cα r.m.s.d. = 6.5 Å). These observations

367   support a likely conserved mechanistic feature, where a hinge-like motion of TM2 is coupled to the

368   conformational state of the NT.

369

370   Several recent connexin structures obtained under a variety of conditions have resolved lipids or

371   detergents within the pore, though the source and conditions favoring their presence has been unclear

372   (Fig. 7c,d)[39]. Similar to Cx46/50, lipids have been modeled at the NT docking site along TM1/2 in Cx36[54,55]

373   and Cx43[53], where their presence correlates with NT displacement from the stabilized open-state

374   observed in Cx46/50 (Fig. 7d). Additionally, stabilized lipids (or detergents) have been identified near the

375   IL binding site of Cx46/50 in other connexin structures, including Cx26[52], Cx36[54,55], and Cx43[53] (Fig. 7d),

376   consistent with the relatively high conservation at these lipid binding sites (Extended Data Fig. 6). While

377   the precise source of lipids from previous studies remains uncertain, these consistent observations

378   suggest a conserved role for lipids in intercalating between subunits and modulating NT conformational

379   states across diverse connexin isoforms.

380

381   **DISCUSSION**

382   Using cryo-EM, we resolved a mosaic of native Cx46/50 gap junction structures under varying pH

383   conditions, uncovering the structural basis of pH-gating (Fig. 8; Supplemental Movie 2). These findings

384   reveal how NT domain conformations and lipid interactions may act synergistically to regulate intercellular

385   communication. However, it is important to note that a direct role of lipids in gap junction gating remains

386   to be validated through cellular functional studies. The observed insertion of lipids into the pore of other

387   connexin isoforms, as well as related innexins[56], pannexins[57], and volume-regulated anion channels[58],

388   suggests this mechanism may have broad physiological relevance to large-pore ion channels. Thus, the

389   dynamic role of lipids in stabilizing gating transitions in Cx46/50 may provide a broad mechanistic

390   foundation for understanding tissue protection during ischemia, connexin-linked pathologies such as age-

391   related cataract formation, and potential therapeutic strategies targeting connexin dysfunction in

392   disease[59].

393

394   *Lipid-mediated pH-gating mechanism of Cx46/50*

395   At neutral pH, Cx46/50 channels predominantly adopt the stabilized open-state, devoid of pore-bound

396   lipids or detergents. Through development of a deep-classification approach, we showed that this state

397   is accompanied by minor populations of a destabilized open-state and a lipid-mediated gated-state at

398   neutral pH (2.6% and 1.0% of particles, respectively) (Fig. 8a,b). Both open states maintain NT domain

399   anchoring to TM1/2 via hydrophobic interactions, maintaining pore diameters sufficient for the permeation

400   of hydrated ions.

401

402 Under mildly acidic conditions, the equilibrium shifts toward the lipid-mediated gated-state (Fig. 8a), with

403 ~67% of subunits adopting a gated conformation, while no fully open channels remain. Although the

404 precise number of gated subunits required for pH-induced junctional uncoupling is unknown, functional

405 studies suggest that a single subunit may be sufficient to trigger transjunctional voltage gating[36]. Thus,

406 the observed cryo-EM ensemble may also align closely with electrophysiology studies which report a

407 majority of channels become gated under similarly acidic conditions[32-35]. Notably, electrophysiology

408 experiments are conducted in the presence of a transjunctional voltage potential, which may further drive

409 closed-state occupancy.

410

411 Under cryo-EM conditions, low pH-induced gating is stabilized by pore-bound lipids (PLs) recruited from

412 the annular lipid environment, filling hydrophobic sites that displace the NT, while interstitial lipids (ILs) at

413 subunit interfaces reinforce TM2-NT interactions. In the absence of lipids, low pH had no structural effect

414 on Cx46/50 (Fig. 3a), underscoring the essential role of lipids in gating. This lipid-mediated process is

415 fully reversible, with lipids translocating back to the surrounding environment upon neutralization (Fig.

416 8a), aligning with the slow kinetics and reversibility observed in functional studies[33,34].

417

418 Our findings, together with prior studies, highlight a coordinated movement of TM2 and the NT, facilitated

419 by a conserved proline kink (P88) that functions as a hinge, conferring TM2 the flexibility to accommodate

420 NT rearrangements in response to pH gating (Fig. 8a,b). The homologous proline in Cx26 and Cx32 has

421 been previously linked to voltage-gating[60,61], suggesting a broader conserved role for NT-TM2 coupling

422 in mediating connexin gating across diverse physiological conditions.

423

424 *Asymmetric and non-cooperative gating*

425 Our findings reveal that NT gating domains operate independently on either side of the intercellular

426 channel, with asymmetrically gated particles resolved at low pH (Fig. 6a; Supplemental Movie 1). This

427 state likely reflects physiological conditions in polarized gap junctions, where gating signals from one

428 coupled cell selectively induces gating on one side of the channel[8,23].

429

430 Further deconvolution of the structural ensemble revealed non-cooperative gating within individual

431 hemichannels, with open and gated NT conformations distributed in a seemingly random pattern (Fig.

432 8c). This behavior aligns with functional studies on Cx32, which suggest that individual subunits can gate

433 independently in response to transjunctional voltage[36]. Similarly, cryo-EM studies of Cx43 and Cx36 have

434 identified non-cooperative NT conformations[53,54]. Collectively, these results support the notion that pH

435 gating of Cx46/50 is more complex than a simple binary transition between fully open and fully closed

436 states, involving an ensemble of gated-states. Future investigations will be necessary to define the

437 minimal number of gated subunits required for complete junctional closure in response to pH.

438

12

439 *Protonation and lipid pathways*

440 Conserved histidine residues, corresponding to H17 and H95 in Cx46/50, are shown to play key roles in

441 pH sensing and gating in several connexins[33,44-46]. Our findings support these previous mutational

442 studies, and suggest protonation of these conserved residues drive lipid interactions and stabilizes the

443 NT in the gated-state, offering mechanistic insights into pH-dependent gating of Cx46/50 that may extend

444 to other connexin isoforms. At low pH, H95 engages in a salt-bridge interaction with the phosphate

445 headgroup of the IL, stabilizing the gated conformation through extensive hydrophobic interactions with

446 the NT and TM2. Intriguingly, the position of the IL at the subunit interface, along with its pH-dependent

447 recruitment to this binding site, suggest a potential pathway for entry or exit of PL lipids (Fig. 4a-c).

448 Similarly, H17 undergoes a pH-dependent shift toward E16, forming a stabilizing salt-bridge with the NT

449 in the gated state (Fig. 4d-f). While these interactions align with the proposed gating mechanism and

450 underscore the importance of conserved histidine residues in pH-gating, further studies are needed to

451 resolve the precise protonation events and explore the potential involvement of non-histidine residues,

452 such as N-terminal acidic residues[62,63]. Additionally, as noted above, the physiological role of lipids in

453 modulating connexin gating remains to be validated in cellular systems, including investigations into

454 potential lipid specificity and translocation pathway into and out of the pore.

455

ACKNOWLEDGEMENTS

AUTHOR CONTRIBUTIONS

J.M.J. designed and executed the nanodisc experiments. J.B.M designed and executed the amphipol experiments. J.M.J. and J.B.M. collected the cryo-EM data. J.M.J. performed image processing and model building. J.M.J. and S.L.R. contributed to data analysis and prepared the initial manuscript. All authors contributed to final revision of the manuscript.

CONFLICT OF INTERESTS

Authors declare no competing interests.

473 **METHODS**

474 *Membrane scaffold protein expression and purification*

475 A plasmid containing the sequence for a histidine tagged MSP1E1 was obtain from Addgene[64] and the

476 protein was expressed and purified as previously described with minor modification[41,65]. Freshly

477 transformed *E.coli* cells (BL21 Gold-DE3, Agilent, Catalog #230130) were grown in LB medium

478 supplemented with 50 µg mL^{-1} kanamycin at 37° C while being shaken at 250 r.p.m. After reaching an

479 OD_{600} of 0.5-0.6, cultures were induced with 0.5 mM IPTG and allowed to express for 3 hrs post-induction

480 at 37° C. Cells were harvested by centrifugation at 4000 x g for 20 min at 4° C and cell pellets were

481 resuspended in ~4 mL per gram of cell pellet of MSP Lysis Buffer (40 mM Tris pH 7.4, 1% Triton X-100,

482 1 mM phenylmethylsulfonyl fluoride (PMSF)). Cell suspensions were flash frozen in liquid nitrogen and

483 stored at -80° C until needed.

484

485 Frozen cell suspensions were supplemented with 1 mM PMSF while thawing on ice and lysed by

486 sonication. Crude lysate was cleared by ultracentrifugation at 150,000 x g for 20 min at 4° C. Sodium

487 chloride was added to the supernatant for a final concentration of 300 mM. The supernatant was filtered

488 (Millipore, 0.22 µm) and applied to a gravity column packed with HisPur Ni-NTA resin (Thermo Fisher

489 Sci) that was prepared with Equilibration buffer (40 mM Tris pH 7.4 and 300 mM NaCl) at a ratio of 1 mL

490 packed resin per gram of cell pellet. The supernatant was batch bound to the resin for 1 hr at 4° C with

491 gentle rocking.

492

493 The MSP-bound resin was washed with 5 column volumes (CV) of Equilibration buffer, followed by 5 CVs

494 of the following buffers: Triton buffer (40 mM Tris pH 8.0, 300 mM NaCl, 1% (vol vol^{-1}) Triton X-100),

495 Equilibration buffer, Cholate buffer (40 mM Tris pH 8.0, 300 mM NaCl, 50 mM cholate), Equilibration

496 buffer, Imidazole Wash Buffer (40 mM Tris pH 8.0, 300 mM NaCl, 50 mM imidazole) and Equilibration

497 buffer. MSP1E1 was eluted from the resin with 3 CV of Elution Buffer (40 mM Tris pH 8.0, 300 mM NaCl,

498 500 mM imidazole).

499

500 Eluate was concentrated to ~5 mg mL^{-1} (UV_{280}) using a 20 kDa m.w.c.o. spin concentrator (Vivaspin 6,

501 Sartorius), filtered (Millipore, 0.22 µm) and applied to a gel filtration column (ENrich SEC 70; BioRad)

502 using a fast protein liquid chromatography (FPLC) (NGC system; BioRad) equilibrated with 20 mM

503 HEPES pH 7.4 and 150 mM NaCl. All chromatography steps were performed at 4° C. Peak fractions

504 were monitored by UV_{280}, pooled and concentrated to 300-500 µM using a 20 kDa m.w.c.o. spin

505 concentrator. Samples were then aliquoted, flash frozen with liquid nitrogen and stored at -80° C until

506 needed.

507

508

509

15

510 *Cx46/50 purification*

511 Native Cx46/50 gap junctions were isolated from sheep lens fiber cells[40,41]. Fresh sheep eyes were

512 obtained from Nebraska Scientific (Omaha, NE). Lenses were removed using a surgical blade and stored

513 at -80° C. After thawing, the core lens fiber tissue, containing Cx46 and Cx50 intercellular channels that

514 are C-terminally truncated (MP38)[42] was dissected from the lens cortical tissue with a surgical blade. The

515 lens core tissue was then Dounce homogenized and stripped membranes were prepared as previously

516 described[40,41]. Stripped membranes were stored at -80° C in Storage Buffer (10 mM Tris pH 8.0, 2 mM

517 EDTA, 2 mM EGTA) at a total protein concentration of 2 mg/mL (BCA, Pierce).

518

519 Thawed membranes were solubilized with 10 mM Tris pH 8.0, 2 mM EDTA, 2 mM EGTA, and 1% (wt

520 vol^{-1}) n-decyl-β-D-maltoside (DM) for 30 min at 37° C with gentle mixing. Insoluble material was cleared

521 by ultracentrifugation 150,000 x g for 30 min at 4° C, followed by filtration (Millipore, 0.22 µm). The

522 supernatant was then separated by anion exchange chromatography at 4° C (UnoQ, BioRad). Buffer A

523 (10 mM Tris pH 8.0, 2 mM EDTA, 2 mM EGTA, 0.3% (wt vol^{-1}) DM) was ran for 20 CV after sample

524 application and protein was eluded with Buffer B (same a Buffer A with the addition of 1 M NaCl) using a

525 gradient elution (to 35% Buffer B) over 20 CV. Peak fractions containing detergent solubilized Cx46/50

526 were concentrated to 150-300 µM as determined by UV$_{280,}$ using a 50 kDa m.w.c.o. spin concentrator

527 (Vivaspin 6, Sartorius).

528

529 *Reconstitution of Cx46/50 into lipid nanodiscs*

530 Freshly prepared Cx46/50 was reconstituted at pH 7.4 into MSP1E1 nanodiscs using dimyristoyl-

531 phosphatidylcholine (DMPC) lipids as previously described[41], with minor modifications. Briefly, chloroform

532 solubilized DMPC (Avanti) was dried under a stream of nitrogen gas creating a thin film and left under

533 vacuum overnight to remove residual solvent. The DMPC thin film was solubilized in 20 mM HEPES pH

534 7.4, 150 mM NaCl and 5% (wt vol^{-1}) DM to a final concentration of 35 mM. Detergent solubilized DMPC

535 was then sonicated two times for 20 mins at 37° C with vortexing in between the sonication steps.

536

537 Solubilized Cx46/50 was mixed with the solubilized DMPC at a molar ratio of 0.6:90 (Cx46/50:DMPC) for

538 60 mins with gentle rotation at 37° C. Purified MSP1E1 was then added for a final molar ratio of 0.6:1:90

539 (Cx46/50:MSP1E1:DMPC) for 15 mins with gentle rotation at 37° C. Detergent was removed with an

540 overnight incubation with SM-2 Bio-Beads (BioRad) at ratio of 30:1 beads:DM (wt:wt) with gentle

541 inversion at 37° C. Bio-beads were removed by filtration and fresh beads were added for an additional

542 60 mins of gentle rotation at 37° C. The beads were removed by filtration and insoluble material was

543 removed by centrifugation at 16,150 x g for 30 mins at 4° C.

544

545 The supernatant at pH 7.4 was filtered (Millipore, 0.22 µm) and applied to an FPLC gel filtration column

546 (Superose 6 Increase 10/300 GL, GE Healthcare) equilibrated with Low pH buffer (20 mM Succinate pH

16

547   5.8, 150 mM NaCl, 2 mM EDTA and 2 mM EGTA). Peak fractions containing Cx46/50 embedded in

548   nanodiscs were combined and concentrated using a 50 kDa m.w.c.o. spin concentrator (Vivaspin 6,

549   Sartorius) to a final concentration of 1.8–2.2 mg mL^{-1} as determined by UV$_{280}$. All chromatography steps

550   were performed at 4° C.

551

552   *Reconstitution of Cx46/50 into amphipol*

553   Freshly purified Cx46/50 was exchanged from DM to amphipol (PMAL-C8, Anatrace) as previously

554   described[40], with minor modification. Peak fractions containing Cx46/50 (determined by SDS-PAGE) from

555   affinity purification (see above) were combined and applied to a gel filtration column (ENrich SEC 650,

556   Bio-Rad) equilibrated with 20 mM HEPES pH 7.4, 150 mM NaCl, 2 mM EDTA, 2 mM EGTA and 0.3%

557   DM (wt vol^{-1}). Peak fractions containing DM solubilized Cx46/50 were pooled and combined with

558   amphipol at a ratio 3:1 amphipol:Cx46/50 (wt:wt). The mixture was gently rotated overnight at 4° C, then

559   Bio-beads were added at a ratio of 30:1 (wt:wt) beads:DM for 60 mins at 4° C with gentle rotation. The

560   beads were removed by filtration and further cleared by centrifugation at 16,150 x g for 30 mins at 4° C.

561   The supernatant containing Cx46/50 in amphipol at pH 7.4 was then filtered (Millipore, 0.22 μm) and then

562   applied to a gel filtration column (ENrich SEC 650, Bio-Rad) equilibrated with Low pH buffer. Peak

563   fractions containing Cx46/50 in amphipol were pooled and spin concentrated (Vivaspin, 50 kDa m.w.c.o.,

564   Satorius) to 1.3 mg mL^{-1}. Protein concentration was determined by UV$_{280}$ and sample purity was assessed

565   by SDS-PAGE. All chromatography was done at 4° C.

566

567   *Controls for lipid mediated pH-gating*

568   After nanodisc reconstitution of Cx46/50 and removal of Bio-beads at pH 7.4, as described above, the

569   sample was then filtered (Millipore, 0.22 μm) and split in half. Half the reconstitution was applied to an

570   FPLC gel filtration column (Superose 6 Increase 10/300 GL, GE Healthcare) equilibrated with Low pH

571   buffer (20 mM Succinate pH 5.8, 150 mM NaCl, 2 mM EDTA and 2 mM EGTA). The other half was

572   applied to a gel filtration column equilibrated with Neutral pH buffer (20 mM HEPES pH 7.4, 150 mM

573   NaCl, 2 mM EDTA and 2 mM EGTA). For each pH condition, peak fractions containing Cx46/50

574   embedded in nanodiscs were combined and concentrated to a final concentration of 1.8-2.2 mg mL^{-1} as

575   determined by UV$_{280}$ using a 50 kDa m.w.c.o. spin concentrator (Vivaspin 6, Sartorius) and sample purity

576   assessed by SDS-PAGE. All chromatography steps were performed at 4° C.

577

578   *Reversible lipid mediated pH-gating*

579   To test whether lipid mediated gating was reversible, fresh Cx46/50 was reconstituted into nanodiscs at

580   pH 7.4 as described above with the minor modification that after reconstitution the entire sample of

581   Cx46/50 embedded in nanodiscs was applied to a gel filtration column (Superose 6, GE Healthcare)

582   equilibrated in Low pH buffer (pH 5.8) to put the channels under gating conditions. Peak fractions

583   containing Cx46/50 embedded in nanodiscs at low pH were pooled, divided in half, and then dialyzed

17

584 (0.5–1 kDa m.w.c.o. Float-A-Lyzer G2; Spectrum Laboratories) overnight at 4° C with gentle stirring in

585 either Neutral pH buffer or Low pH buffer (control). The ratio of dialysis buffer to sample was 100:1

586 (vol:vol). Dialysis buffer was exchanged after 2 hrs, and again after dialyzing overnight at 4° C with gentle

587 stirring. After 2 hrs of dialysis with fresh buffer the following morning the sample was recovered and

588 concentrated to 1.8–2.1 mg mL^{-1} as determined by UV$_{280}$, using a spin concentrator (Vivaspin, 50 kDa

589 m.w.c.o., Satorius).

590

591 *Negative stain electron microscopy*

592 Cx46/50 embedded into lipid nanodiscs or solubilized with amphipol were prepared for negative stain

593 EM, as previously described[40,41]. Briefly, 3 µL of sample (~0.02 mg mL^{-1}) was applied to a glow-

594 discharged continuous carbon coated EM grid (Ted Pella, G400), blotted with filter paper and washed

595 three times with gel filtration buffer. The sample was then stained with freshly prepared uranyl formate

596 (0.75% wt vol^{-1}, SPI-Chem). Negatively stained specimens were imaged on a 120 kV TEM (iCorr, Thermo

597 Fisher Scientific) at a nominal 49,000 x magnification at the specimen level using a 2k x 2k CCD camera

598 (Eagle 2 K TEM CCD, Thermo Fisher Scientific) with calibrated pixel size of 4.37 Å and with a nominal

599 defocus of -1.5 µm, performed at OHSU's Multiscale Microscopy Core.

600

601 *Cryo-EM specimen preparation and data collection*

602 Samples were prepared for cryo-EM using 3 µL of freshly purified Cx46/50 embedded in nanodisc (1.8–

603 2.2 mg mL^{-1}) or amphipol (1.3 mg mL^{-1}) applied to glow-discharged holey carbon grids (Quantifoil,

604 R1.2/1.3 or R2/1). All cryo-samples were vitrified using a Vitrobot Mark IV (Thermo Fisher Scientific) at

605 20° C with 100% humidity and were blotted for 4–4.5 sec prior to being plunged into liquid ethane and

606 stored in liquid nitrogen.

607

608 All cryo-EM specimens were imaged at the Pacific Northwest Cryo-EM Center (PNCC) on a Titan G4

609 Krios cryo-TEM (Thermo Fisher) operated at 300 kV. Movies for the amphipol dataset were recorded on

610 a Gatan K2 summit direct electron detector at a nominal magnification of 29,000x (calibrated pixel size =

611 0.665 Å pixel^{-1}) in counting mode, with an energy filter set to a 20 eV slit width. Nanodisc datasets were

612 collected on a Gatan K3 direct electron detector at 29,000x or 105,000x nominal magnification (calibrated

613 pixel size = 0.788 or 0.822 Å pixel^{-1}) in super resolution mode, with energy filter slit widths of 10-20 eV.

614 Data collections used 45 to 55 frames and total doses ranged from 40–50 e^{-} Å^{-2}. Datasets of 555–12423

615 movies were collected using SerialEM[66], with nominal defocus ranges of -0.8 to -2.2 µm or -0.5 to -1.8

616 µm. See Extended Data Table 1 for details of each dataset.

617

618 *Cryo-EM image processing*

619 All datasets were processed in CryoSPARC (v4.4.1)[67] and pre-processing was carried out in the same

620 fashion across all datasets. Dose weighting and beam induced motion correction were done using Patch

18

621 motion correction. Micrographs were binned to their nominal pixel size (2x super resolution pixel size)

622 during Patch motion correction, here on referred to as the unbinned pixel size. Contrast transfer function

623 (CTF) estimation was performed by Patch CTF estimation.

624

625 All datasets were processed using the same routine and the same masks used across datasets.

626 Processing of Cx46/50 at low pH embedded in DMPC nanodiscs (Collection #1) will be described in detail

627 as the representative dataset. Details for individual datasets are shown in the image processing workflow

628 (Extend Data Fig. 3, 7-9). Using a subset of micrographs, semi-automated particle picking was used to

629 create a preliminary 3D reconstruction for template particle picking on the entire dataset, resulting in

630 5,572,213 particle picks from 7,072 micrographs. After multiple rounds of 2D classification and removing

631 duplicate particles, 685,022 bona-fide particles (binned to 2.4 Å pixel^{-1}) were selected to generate an *ab-*

632 *initio* model.

633

634 This was followed by a round of homogeneous refinement using D6 symmetry, unbinning of the particles

635 (to 0.802 Å pixel^{-1}) and a round of non-uniform refinement (D6 symmetry) leading to a 2.14 Å consensus

636 reconstruction. The particles and map from the consensus refinement were used in heterogenous

637 refinement with 6 classes (D6 symmetry) with a target resolution of 4 Å. Non-uniform refinements were

638 then applied to all six classes, independently, using unbinned particle stacks and applying D6 symmetry.

639 Particle stacks from 3D refinements that went below 3 Å (classes #0, #1 and #4, 476,719 particles total)

640 were combined, down sampled (1.54 Å pixel^{-1}, box 200 pixels) and subjected to another round of non-

641 uniform refinement (D6 symmetry) resulting in a 3.16 Å resolution 3D reconstruction. The variability of

642 this down sampled stack of particles was then assessed at the whole particle level by 3D Variability

643 Analysis (3DVA)[51] to guide the classification of various states for final 3D refinement.

644

645 *3D variability analysis and classification of states*

646 3DVA in CryoSPARC was used to parse through the conformational heterogeneity in the NT-gating

647 domain at the gap junction level, and classify the gated-, destabilized open- and stabilized open-states.

648 The particle stack from the binned non-uniform refinement (box 200 pixels, 1.54 Å/pix) was symmetry

649 expanded using D6 symmetry yielding a particle stack of 5,720,628 particles prior to 3DVA. A custom 10

650 Å low-pass filtered mask that excluded the nanodisc was generated in CryoSPARC with an 8 Å resolution

651 molmap created in ChimeraX using Cx46 (7JKC) that had additional residues placed into the pore to

652 generate density to cover the channel entrances. 3DVA was performed using a target resolution of 4 Å,

653 principal components (PC) of interest were selected and further analyzed. Ultimately in every dataset the

654 primary PC was analyzed, as well as PCs that demonstrated asymmetric gating (Collections #4 and #5).

655

656 The intermediate 3DVA display job type was then used to classify the states of interest. The 3DVA display

657 job was used to separate the PC into nine frames by setting the rolling window to zero and outputting

19

658   particle subsets, generating unique stack of particles along the PC of interest. Each frame's particle stack

659   was independently locally refined (D6 symmetry) using the same mask used for 3DVA, duplicate particles

660   were removed, and then particles were unbinned for a final round of non-uniform refinement with D6

661   symmetry applied. Particle stacks yielding reconstructions of similar states (i.e., similar NT conformation)

662   were then combined. Three distinct states were identified (gated, destabilized open and stabilized open)

663   and used for model building. The stabilized open-state map had a final resolution of 2.5 Å with 42,646

664   particles, the destabilized open-state map had a final resolution of 2.2 Å with 218,088 particles, and the

665   gated-state map had a final resolution of 2.2 Å with 198,875 particles (gold-standard FSC) (Extended

666   Data Table 1).

667

668   *Merging cryo-EM datasets for identification of rare neutral pH states*

669   To computationally isolate rare states at neutral pH, datasets from neutral and low pH conditions were

670   merged and subjected to 3DVA. This was achieved by merging cryoEM datasets samples that were

671   prepped from the same specimen, collected on the same cryo-electron microscope with the same

672   settings (*i.e.,* Collections #3 and #4 were merged and Collections #5 and #6 were merged). As an

673   example, Collections #5 and #6, belonging to the reversible lipid mediated pH-gating experiment will be

674   described in detail. The unbinned particle stacks (0.8016 Å pixel^{-1}, box 384 pixels) obtained after

675   heterogenous refinement from the respective datasets were merged. The low pH control dataset

676   (Collection #5) contributed 764,205 particles and the neutral pH particle stack (Collection #6) contributed

677   427,873 particles, for a total of 1,192,078 particles.

678

679   The merged unbinned particle stack was down sampled (box 160, 1.97 Å/pix) and subjected to a round

680   of non-uniform refinement (D6 symmetry), and then symmetry expanded using D6 symmetry for a total

681   of 14,304,936 particles prior to 3DVA. The symmetry expanded particles were then analyzed by 3DVA

682   with a target resolution of 4 Å, using the same mask used for the 3DVA on the independent datasets

683   described above. PCs of interest were split into 9 frames/particle stacks along a PC using the

684   intermediates 3DVA display output. Each particle stack was independently locally refined using particles

685   from both low and neutral pH datasets. The particles were then reverted to their original datasets, and

686   then deduplicated to undo symmetry expansion.

687

688   The particles were then unbinned and individual particles stacks were subjected to non-uniform

689   refinement (D6 symmetry). Particles stacks demonstrating similar states were pooled and a final round

690   of non-uniform refinement (D6 symmetry) was performed. Using this approach, all three states (gated,

691   destabilized open and stabilized open) were identified in the neutral pH datasets revealing rare

692   populations of gated-state gap junctions at neutral pH (1% for Collection #2 and 4% for Collection #5),

693   which were previously not observed in these datasets using other common approaches of 3D

694   classification. To assess for influence of initial map bias on end state maps, initial maps of open and

20

695 gated states and initial low pass filters (16 Å) were both assayed as starting models, yielding similar
696 results.

697

698 *Subunit classification*

699 Subunit-level heterogeneity was analyzed using signal subtraction and 3D classification in CryoSPARC.
700 This workflow was applied to particles from Collections #1, #3, #4, #5 and #6. The description here
701 focuses on the workflow for Collection #4, as the exemplar approach.

702

703 A non-uniform refinement particle stack containing 476,719 high-resolution particles was down sampled
704 by 2x binning (1.6 Å pixel^{-1}, 240-pixel box size). A subset of 100,000 randomized particles (~21% of the
705 total) was symmetry expanded (D6 symmetry), generating 1.2 million particles that were then subjected
706 to local refinement using D6 symmetry. A mask for signal subtraction was generated in ChimeraX by
707 creating an 8 Å molecular map (molmap), generated from overlaid monomer models of the stabilized
708 open and gated states. After signal subtraction, particles were re-centered and subjected to 3D
709 classification without alignment. Classification parameters were optimized as follows: three classes, a
710 target resolution of 3 Å, an O-EM learning rate of 0.3, an O-EM batch size of 2,000 particles, no per-
711 particle scale factors, an initial low-pass filter resolution of 8 Å, and hard classification. Open and gated
712 states were distinguished based on the position of the NT gating domain.

713

714 To determine the distribution of open and gated-state monomers within gap junction particles, metadata
715 from the signal-subtracted 3D classified particles was analyzed. The following metadata fields were
716 extracted into a CSV file from each class's exported particle .cs file: uid, sym_expand/idx, and
717 sym_expand/src_uid. Metadata from similar classes were combined to generate concatenated files,
718 representing open and gated states, respectively.

719

720 The frequency of open and gated-states within gap junction particles and hemichannels was analyzed
721 independently. An in-house developed bash script, "*Subunit State Frequency*", was used to calculate the
722 frequency of 'sym_expand/src_uid' occurrences to determine the distribution of open and gated
723 monomers in gap junctions. For example, if a gated monomer's 'sym_expand/src_uid' appeared 4 times,
724 then 4 of the 12 subunits in the gap junction were classified as gated. To analyze hemichannels, another
725 custom bash script, "*Gap Junction Splitter*", was employed to split gap junction particles into their
726 respective hemichannels based on the 'sym_expand/idx' metadata. The resulting hemichannel metadata
727 was then processed using the same *Subunit State Frequency* script to evaluate the distribution of open
728 and gated monomers within the individual hemichannels of the parent gap junction particles. Frequency
729 data for both gap junctions and hemichannels were subsequently plotted to visualize the distribution of
730 gated states across the dataset.

731

732 To investigate potential cooperativity of subunit gating across hemichannels within gap junction particles,
733 a custom bash script, "*Hemichannel Arrangement*", was developed to identify the relative positions of
734 open/gated conformers and applied to the gated-state particle metadata. Initially, gap junction particle
735 metadata was split into hemichannels using the *Gap Junction Splitter* script described above.
736 Subsequently, the metadata for each hemichannel was analyzed independently to evaluate the relative
737 positions of gated subunits in hemichannels containing two, three, or four gated subunits. The
738 *Hemichannel Arrangement* script determined the number of gated subunits in each hemichannel by
739 counting the occurrences of unique 'sym_expand/src_uid' IDs. For hemichannels with two to four gated
740 subunits, the script analyzed the specific arrangements of gated subunits based on the combination of
741 'sym_expand/idx' IDs. Each unique arrangement was tallied to quantify the distribution of gated-state
742 configurations within the hemichannel metadata. These results provided insights into the spatial
743 organization and potential cooperativity of subunit gating across the hemichannels.

744

745 *Atomic modeling and validation*
746 Previously published models of Cx46 (7JKC) and Cx50 (7JJP) in the stabilized open-state were used as
747 starting points for atomic modeling in Coot[68]. For the gated and destabilized open-states, the NT domains
748 were pruned to the 20th residue and rebuilt into the respective maps. To avoid bias, all histidine were
749 modeled in the protonated state for low pH datasets. Models were then iteratively refined in Phenix[69] and
750 Coot until convergence of statistics determined by MolProbity[70]. After the Cx46 models statistics
751 converged, point mutations were introduced in Coot to convert to the Cx50 isoform and the model
752 refinement/validation process was repeated until convergence (Extended Data Table 1).

753

754 Structural analysis and visualization of Coulombic surface potentials were performed in ChimeraX[71]. Pore
755 profiles were analyzed using the program HOLE[72]. For this analysis, the sidechain of R9 on Cx46 (7JKC)
756 was pruned to $C\beta$ to account for the dynamic nature of this residue as demonstrated *in silco*[26] and the
757 weak density for the sidechain in the original cryo-EM map[41]. Sequence alignments were created using
758 Clustal-w[73] and visualized in Jalview[74].

759

760 *AI-assisted technologies*
761 During the development of this work ChatGPT (OpenAI) was used for help in writing code and to revise
762 portions of the text to improve clarity. After using this tool for coding, synthetic datasets were generated
763 and used for testing and validation. The authors reviewed and edited any content that was generated
764 with this tool and take full responsibility of the content of this publication.

765

766

767

DATA AVAILABILITY

Cryo-EM maps have been deposited to the Electron Microscopy Data Bank under accession codes EMDB-XXXXX (stable-open Cx46/50 at pH 5.8), EMDB-XXXXX (destabilized-open Cx46/50 at pH 5.8), EMDB-XXXXX (gated Cx46/50 at pH 5.8), EMDB-XXXXX (stable-open Cx46/50 at pH 7.4), EMDB-XXXXX (destabilized-open Cx46/50 at pH 7.4), EMDB-XXXXX (gated Cx46/50 at pH 7.4), EMDB-XXXXX (asymmetric gated Cx46/50 at pH 5.8) and EMDB-XXXXX (open Cx46/50 at pH 5.8 in amphipol). Coordinates for Cx46 atomic models have been deposited to the Protein Data Bank under accession codes XXXX (stable-open Cx46 at pH 5.8), XXXX (destabilized-open Cx46 at pH 5.8), XXXX (gated Cx46 at pH 5.8), XXXX (stable-open Cx46 at pH 7.4), XXXX (destabilized-open Cx46 at pH 7.4), XXXX (gated Cx46 at pH 7.4), XXXX (asymmetric gated Cx46 at pH 5.8) and XXXX (stable-open Cx46 at pH 5.8 in amphipol). Coordinates for Cx50 atomic models have been deposited to the Protein Data Bank under accession codes XXXX (stable-open Cx50 at pH 5.8), XXXX (destabilized-open Cx50 at pH 5.8), XXXX (gated Cx50 at pH 5.8), XXXX (stable-open Cx50 at pH 7.4), XXXX (destabilized-open Cx50 at pH 7.4), XXXX (gated Cx50 at pH 7.4), XXXX (asymmetric gated Cx50 at pH 5.8) and XXXX (stable-open Cx50 at pH 5.8 in amphipol). The original multi-frame micrographs have been deposited to EMPIAR under accession codes EMPIAR -XXXXXX (Collection #1, Cx46/50 at pH 5.8 in nanodiscs), EMPIAR -XXXXXX (Collection #2, Cx46/50 at pH 5.8 in amphipol), EMPIAR -XXXXXX (Collection #3, Cx46/50 at pH 7.4 in nanodiscs), EMPIAR -XXXXXX (Collection #4, Cx46/50 at pH 5.8 in nanodiscs), EMPIAR -XXXXXX (Collection #5, Cx46/50 at pH 5.8 in nanodiscs) and EMPIAR -XXXXXX (Collection #6, reversibly gated Cx46/50 at pH 7.4 in nanodiscs).

CODE AVAILABILITY

In-house code developed for the analysis of image processing meta data have been deposited on the Reichow Lab GitHub repository (https://github.com/reichow-lab/subunit_analysis).

REFERENCES

1. Goodenough, D.A. & Paul, D.L. Gap junctions. *Cold Spring Harb Perspect Biol* **1**, a002576 (2009).

2. Lucaciu, S.A., Leighton, S.E., Hauser, A., Yee, R. & Laird, D.W. Diversity in connexin biology. *J Biol Chem* **299**, 105263 (2023).

3. Delmar, M. et al. Connexins and Disease. *Cold Spring Harb Perspect Biol* (2017).

4. Garcia, I.E. et al. Connexinopathies: a structural and functional glimpse. *BMC Cell Biol* **17 Suppl 1**, 17 (2016).

5. Aasen, T., Mesnil, M., Naus, C.C., Lampe, P.D. & Laird, D.W. Gap junctions and cancer: communicating for 50 years. *Nat Rev Cancer* **16**, 775-788 (2016).

6. Andrade-Rozental, A.F. et al. Gap junctions: the "kiss of death" and the "kiss of life". *Brain Res Brain Res Rev* **32**, 308-15 (2000).

7. Spray, D.C., Hanstein, R., Lopez-Quintero, S. V., Stout, R. F., Suadicani, S. O., Thi, M. M. Gap junctions and Bystander effects: Good Samaritans and executioners. *Wiley Interdisciplinary Reviews: Membrane Transport and Signaling* **2**, 1-15 (2013).

8. Harris, A.L., Spray, D.C. & Bennett, M.V. Kinetic properties of a voltage-dependent junctional conductance. *J Gen Physiol* **77**, 95-117 (1981).

9. Spray, D.C., Harris, A.L. & Bennett, M.V. Equilibrium properties of a voltage-dependent junctional conductance. *Journal of General Physiology* **77**, 77-93 (1981).

10. Turin, L. & Warner, A. Carbon dioxide reversibly abolishes ionic communication between cells of early amphibian embryo. *Nature* **270**, 56-7 (1977).

11. Spray, D.C., Harris, A.L. & Bennett, M.V. Gap junctional conductance is a simple and sensitive function of intracellular pH. *Science* **211**, 712-5 (1981).

12. Rose, B. & Loewenstein, W.R. Permeability of cell junction depends on local cytoplasmic calcium activity. *Nature* **254**, 250-2 (1975).

13. Oliveira-Castro, G.M. & Loewenstein, W.R. Junctional membrane permeability : Effects of divalent cations. *J Membr Biol* **5**, 51-77 (1971).

14. Loewenstein, W.R., Nakas, M. & Socolar, S.J. Junctional membrane uncoupling. Permeability transformations at a cell membrane junction. *J Gen Physiol* **50**, 1865-91 (1967).

15. Contreras, J.E. et al. Role of connexin-based gap junction channels and hemichannels in ischemia-induced cell death in nervous tissue. *Brain Res Brain Res Rev* **47**, 290-303 (2004).

16. Dhein, S. Cardiac ischemia and uncoupling: gap junctions in ischemia and infarction. *Adv Cardiol* **42**, 198-212 (2006).

17. Mathias, R.T., White, T.W. & Gong, X. Lens gap junctions in growth, differentiation, and homeostasis. *Physiol Rev* **90**, 179-206 (2010).

18. Kistler, J. et al. Connexins in the lens: are they to blame in diabetic cataractogenesis? *Novartis Found Symp* **219**, 97-108; discussion 108-12 (1999).

19. Khan, A.K. et al. A Steric "Ball-and-Chain" Mechanism for pH-Mediated Regulation of Gap Junction Channels. *Cell Rep* **31**, 107482 (2020).

20. Sohl, G. & Willecke, K. Gap junctions and the connexin protein family. *Cardiovasc Res* **62**, 228-32 (2004).

21. Sosinsky, G.E. & Nicholson, B.J. Structural organization of gap junction channels. *Biochim Biophys Acta* **1711**, 99-125 (2005).

22. Harris, A.L. Connexin channel permeability to cytoplasmic molecules. *Prog Biophys Mol Biol* **94**, 120-43 (2007).

23. Verselis, V.K., Ginter, C.S. & Bargiello, T.A. Opposite voltage gating polarities of two closely related connexins. *Nature* **368**, 348-51 (1994).

24. Kronengold, J., Srinivas, M. & Verselis, V.K. The N-terminal half of the connexin protein contains the core elements of the pore and voltage gates. *The Journal of membrane biology* **245**, 453-63 (2012).

25. Xin, L., Gong, X.Q. & Bai, D. The role of amino terminus of mouse Cx50 in determining transjunctional voltage-dependent gating and unitary conductance. *Biophys J* **99**, 2077-86 (2010).

26. Yue, B. et al. Connexin 46 and connexin 50 gap junction channel properties are shaped by structural and dynamic features of their N-terminal domains. *J Physiol* **599**, 3313-3335 (2021).

27. Liu, S. et al. A structural basis for the unequal sensitivity of the major cardiac and liver gap junctions to intracellular acidification: the carboxyl tail length. *Biophys J* **64**, 1422-33 (1993).

28. Ek-Vitorin, J.F. et al. PH regulation of connexin43: molecular analysis of the gating particle. *Biophys J* **71**, 1273-84 (1996).

29. Morley, G.E., Taffet, S.M. & Delmar, M. Intramolecular interactions mediate pH regulation of connexin43 channels. *Biophys J* **70**, 1294-302 (1996).

30. Lin, J.S., Eckert, R., Kistler, J. & Donaldson, P. Spatial differences in gap junction gating in the lens are a consequence of connexin cleavage. *Eur J Cell Biol* **76**, 246-50 (1998).

31. Xu, X., Berthoud, V.M., Beyer, E.C. & Ebihara, L. Functional role of the carboxyl terminal domain of human connexin 50 in gap junctional channels. *J Membr Biol* **186**, 101-12 (2002).

32. Stergiopoulos, K. et al. Hetero-domain interactions as a mechanism for the regulation of connexin channels. *Circ Res* **84**, 1144-55 (1999).

33. Trexler, E.B., Bukauskas, F.F., Bennett, M.V., Bargiello, T.A. & Verselis, V.K. Rapid and direct effects of pH on connexins revealed by the connexin46 hemichannel preparation. *J Gen Physiol* **113**, 721-42 (1999).

34. Eckert, R. pH gating of lens fibre connexins. *Pflugers Arch* **443**, 843-51 (2002).

35. DeRosa, A.M., Mui, R., Srinivas, M. & White, T.W. Functional characterization of a naturally occurring Cx50 truncation. *Invest Ophthalmol Vis Sci* **47**, 4474-81 (2006).

36. Oh, S., Abrams, C.K., Verselis, V.K. & Bargiello, T.A. Stoichiometry of transjunctional voltage-gating polarity reversal by a negative charge substitution in the amino terminus of a connexin32 chimera. *J Gen Physiol* **116**, 13-31 (2000).

37. Peracchia, C. & Peracchia, L.L. Inversion of both gating polarity and CO2 sensitivity of voltage gating with D3N mutation of Cx50. *Am J Physiol Cell Physiol* **288**, C1381-9 (2005).

38. Bargiello, T.A., Tang, Q., Oh, S. & Kwon, T. Voltage-dependent conformational changes in connexin channels. *Biochim Biophys Acta* **1818**, 1807-22 (2012).

39. Jagielnicki, M., Kucharska, I., Bennett, B.C., Harris, A.L. & Yeager, M. Connexin Gap Junction Channels and Hemichannels: Insights from High-Resolution Structures. *Biology (Basel)* **13**(2024).

40. Myers, J.B. et al. Structure of native lens connexin 46/50 intercellular channels by cryo-EM. *Nature* **564**, 372-377 (2018).

41. Flores, J.A. et al. Connexin-46/50 in a dynamic lipid environment resolved by CryoEM at 1.9 A. *Nat Commun* **11**, 4331 (2020).

42. Kistler, J., Schaller, J. & Sigrist, H. MP38 contains the membrane-embedded domain of the lens fiber gap junction protein MP70. *J Biol Chem* **265**, 13357-61 (1990).

43. Wang, Z. & Schey, K.L. Phosphorylation and truncation sites of bovine lens connexin 46 and connexin 50. *Exp Eye Res* **89**, 898-904 (2009).

44. Sanchez, H.A., Bienkowski, R., Slavi, N., Srinivas, M. & Verselis, V.K. Altered inhibition of Cx26 hemichannels by pH and Zn2+ in the A40V mutation associated with keratitis-ichthyosis-deafness syndrome. *J Biol Chem* **289**, 21519-32 (2014).

45. Gonzalez-Nieto, D. et al. Regulation of neuronal connexin-36 channels by pH. *Proc Natl Acad Sci U S A* **105**, 17169-74 (2008).

46. Ek, J.F., Delmar, M., Perzova, R. & Taffet, S.M. Role of histidine 95 on pH gating of the cardiac gap junction protein connexin43. *Circ Res* **74**, 1058-64 (1994).

47. Bukauskas, F.F. & Peracchia, C. Two distinct gating mechanisms in gap junction channels: CO2-sensitive and voltage-sensitive. *Biophys J* **72**, 2137-42 (1997).

48. Srinivas, M. et al. Voltage dependence of macroscopic and unitary currents of gap junction channels formed by mouse connexin50 expressed in rat neuroblastoma cells. *J Physiol* **517 (Pt 3)**, 673-89 (1999).

49. Hopperstad, M.G., Srinivas, M. & Spray, D.C. Properties of gap junction channels formed by Cx46 alone and in combination with Cx50. *Biophys J* **79**, 1954-66 (2000).

50. Srinivas, M., Kronengold, J., Bukauskas, F.F., Bargiello, T.A. & Verselis, V.K. Correlative studies of gating in Cx46 and Cx50 hemichannels and gap junction channels. *Biophys J* **88**, 1725-39 (2005).

51. Punjani, A. & Fleet, D.J. 3D variability analysis: Resolving continuous flexibility and discrete heterogeneity from single particle cryo-EM. *J Struct Biol* **213**, 107702 (2021).

52. Brotherton, D.H., Savva, C.G., Ragan, T.J., Dale, N. & Cameron, A.D. Conformational changes and CO(2)-induced channel gating in connexin26. *Structure* **30**, 697-706 e4 (2022).

53. Lee, H.J. et al. Conformational changes in the human Cx43/GJA1 gap junction channel visualized using cryo-EM. *Nat Commun* **14**, 931 (2023).

54. Lee, S.N. et al. Cryo-EM structures of human Cx36/GJD2 neuronal gap junction channel. *Nat Commun* **14**, 1347 (2023).

55. Mao, W. & Chen, S. Assembly mechanisms of the neuronal gap junction channel connexin 36 elucidated by Cryo-EM. *Arch Biochem Biophys* **754**, 109959 (2024).

56. Burendei, B. et al. Cryo-EM structures of undocked innexin-6 hemichannels in phospholipids. *Sci Adv* **6**, eaax3157 (2020).

57. Kuzuya, M. et al. Structures of human pannexin-1 in nanodiscs reveal gating mediated by dynamic movement of the N terminus and phospholipids. *Sci Signal* **15**, eabg6941 (2022).

58. Kern, D.M. et al. Structural basis for assembly and lipid-mediated gating of LRRC8A:C volume-regulated anion channels. *Nat Struct Mol Biol* **30**, 841-852 (2023).

59. Laird, D.W. & Lampe, P.D. Therapeutic strategies targeting connexins. *Nat Rev Drug Discov* **17**, 905-921 (2018).

60. Suchyna, T.M., Xu, L.X., Gao, F., Fourtner, C.R. & Nicholson, B.J. Identification of a proline residue as a transduction element involved in voltage gating of gap junctions. *Nature* **365**, 847-9 (1993).

61. Ri, Y. et al. The role of a conserved proline residue in mediating conformational changes associated with voltage gating of Cx32 gap junctions. *Biophys J* **76**, 2887-98 (1999).

62. Rimkute, L. et al. Modulation of Connexin-36 Gap Junction Channels by Intracellular pH and Magnesium Ions. *Front Physiol* **9**, 362 (2018).

63. Wang, X. et al. pH-dependent channel gating in connexin26 hemichannels involves conformational changes in N-terminus. *Biochim Biophys Acta* **1818**, 1148-57 (2012).

933   64.   Denisov, I.G., Grinkova, Y.V., Lazarides, A.A. & Sligar, S.G. Directed self-assembly of
934   monodisperse phospholipid bilayer Nanodiscs with controlled size. *J Am Chem Soc* **126**, 3477-
935   87 (2004).

936   65.   Ritchie, T.K. et al. Chapter 11 - Reconstitution of membrane proteins in phospholipid bilayer
937   nanodiscs. *Methods Enzymol* **464**, 211-31 (2009).

938   66.   Mastronarde, D.N. Automated electron microscope tomography using robust prediction of
939   specimen movements. *J Struct Biol* **152**, 36-51 (2005).

940   67.   Punjani, A., Rubinstein, J.L., Fleet, D.J. & Brubaker, M.A. cryoSPARC: algorithms for rapid
941   unsupervised cryo-EM structure determination. *Nat Methods* **14**, 290-296 (2017).

942   68.   Casanal, A., Lohkamp, B. & Emsley, P. Current developments in Coot for macromolecular model
943   building of Electron Cryo-microscopy and Crystallographic Data. *Protein Sci* **29**, 1069-1078
944   (2020).

945   69.   Adams, P.D. et al. PHENIX: a comprehensive Python-based system for macromolecular structure
946   solution. *Acta Crystallogr.* **D66**, 213-221 (2010).

947   70.   Chen, V.B. et al. MolProbity: all-atom structure validation for macromolecular crystallography.
948   *Acta Crystallogr D Biol Crystallogr* **66**, 12-21 (2010).

949   71.   Goddard, T.D. et al. UCSF ChimeraX: Meeting modern challenges in visualization and analysis.
950   *Protein Sci* **27**, 14-25 (2018).

951   72.   Smart, O.S., Neduvelil, J.G., Wang, X., Wallace, B.A. & Sansom, M.S. HOLE: a program for the
952   analysis of the pore dimensions of ion channel structural models. *Journal of molecular graphics*
953   **14**, 354-60, 376 (1996).

954   73.   Larkin, M.A. et al. Clustal W and Clustal X version 2.0. *Bioinformatics* **23**, 2947-8 (2007).

955   74.   Procter, J.B. et al. Alignment of Biological Sequences with Jalview. *Methods Mol Biol* **2231**, 203-
956   224 (2021).
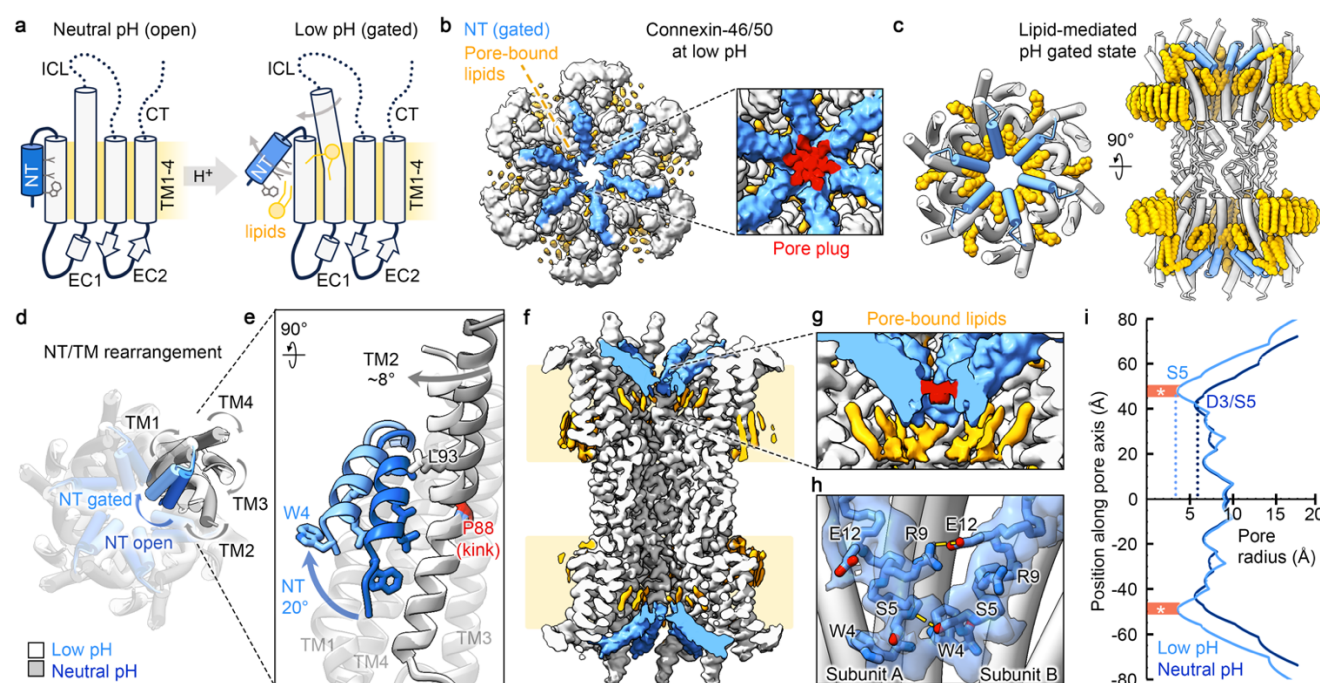
957

958

MAIN FIGURES AND LEGENDS

Figure 1

Figure 1. Low pH gated-state of connexin-46/50. a Schematic illustrating the pH-gating mechanism, where lipids stabilize the N-terminal domain (NT) in the gated-state upon acidification. **b** Cryo-EM map and **c** atomic model of Cx46/50 at low pH, highlighting the NT (light blue) and lipids (orange). Inset in panel b, shows a plug-like NT density observed at lower map thresholds (red), indicating complete pore occlusion. Lipids are observed within the pore lumen and at subunit interfaces, stabilizing the gated-state conformation. **d** Overlay of the previously described stabilized open-state (7JKC, TMs – grey, NT – dark blue) and the low pH gated-state (TMs – white, NT – light blue) showing concerted NT and TM movements induced by acidification. **e** Zoomed view of overlayed subunits, illustrating a 20° displacement of the NT toward the pore and rearrangement of hydrophobic residues (W4, L7 and L11). TM2 is displaced by approximately 8°, facilitated by a conserved proline kink (P88, red), maintaining hydrophobic contact between L93 (V93 in Cx50) and A14 (V14 in Cx50) on the NT. **f** Slice view of the cryo-EM map, showing lipids resolved within the channel pore, stabilizing the NT gated-state. **g** Inset, displaying the map at lower contour levels to highlight the pore plug and pore-bound lipid densities. **h** Close-up of NT gating domains with inter-subunit electrostatic interactions shown. The cryo-EM map for the NTs (blue transparency) showing fit of the model to the map features. **i** Pore profile plot comparing pore radii of low and neutral pH models, noting the proximal NT residues G2 and D3 are absent in the Cx46/50 low pH model. Regions associated with the unmodeled NT plug density are indicated (red; asterisk). Structural models display Cx46 as the representative isoform.
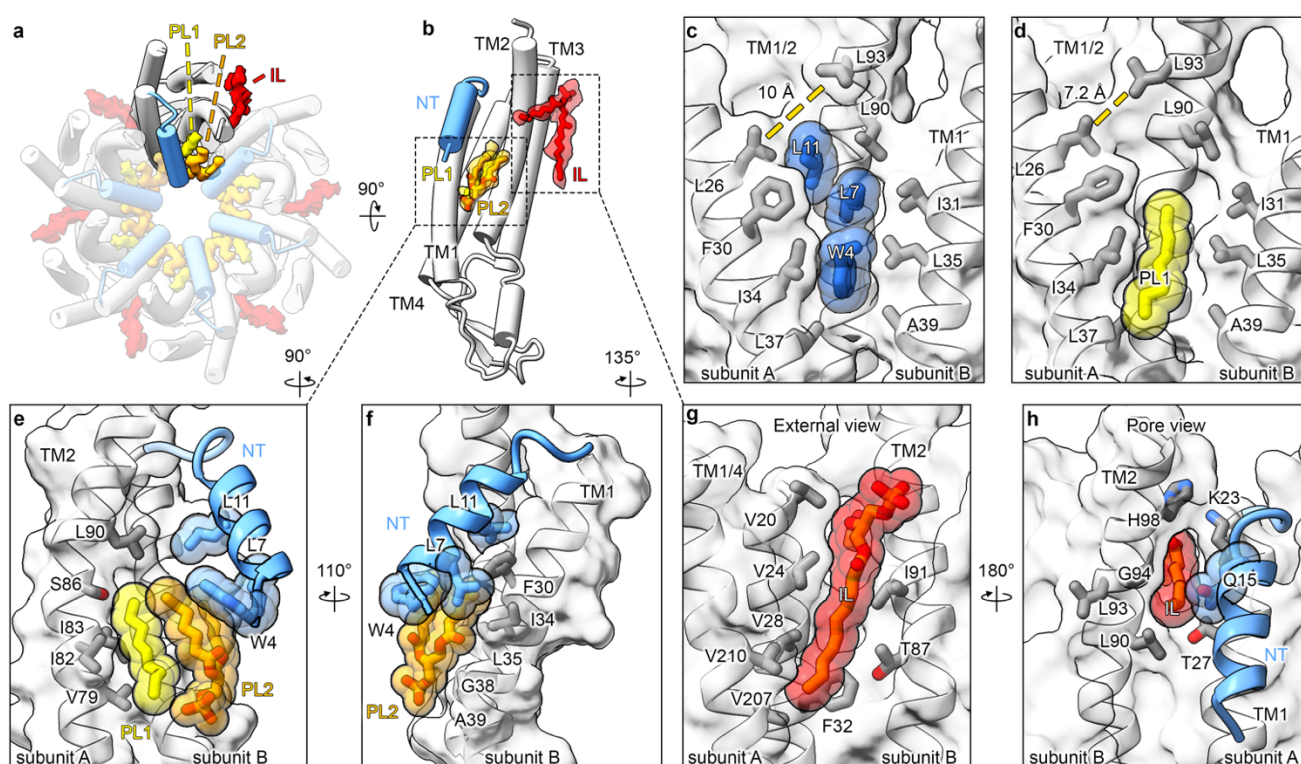
28

Figure 2

Figure 2. Lipid stabilization of the pH gated-state. a Cytoplasmic view of the Cx46/50 gated-state model showing segmented densities for the pore-bound lipids PL1 and PL2 (yellow and orange, respectively) forming a hydrophobic "gasket" that stabilizes the gated NT (light blue). Interstitial lipid (IL) densities (red) are intercalated between connexin subunits. **b** Single subunit view with modeled PL and IL lipids (stick representation) fitted to their respective segmented densities. **c** Zoomed view of Cx46 showing the NT hydrophobic residues (W4, L7 and L11) in the stabilized open-state at neutral pH (dark blue), anchored into the hydrophobic cleft formed by TM1/2 (grey sidechains). **d** At low pH, PL1 (yellow) occupies the NT anchoring site, and TM2 shifts 2.8 Å closer to TM1 compared to the neutral pH open-state (measured between L93 and L26, dotted lines). **e,f** Close-ups showing PL1 and PL2 inserted beneath the NT, supporting the gated-state through hydrophobic complementarity with TM1/2, with interacting amino acid sidechains labeled. **g,h** Views of IL intercalated between subunits, extending from the intracellular leaflet of the nanodisc lipid bilayer (g) toward the channel pore forming interactions with TM2 and the NT (h). Panels c-h display models of Cx46 as the representative isoform.
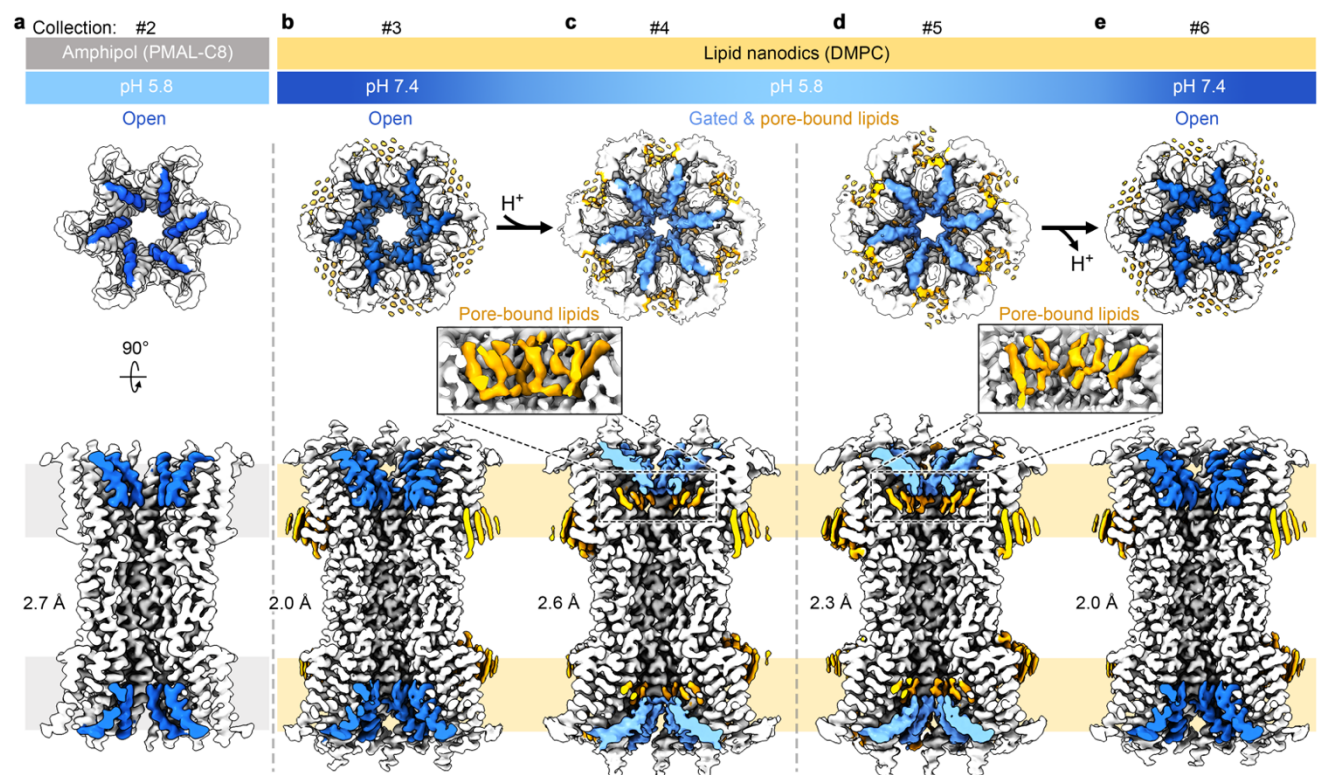
29

1002 **Figure 3**

1003

1004 **Figure 3. Lipid requirement and reversibility in the pH-gating mechanism.** Cryo-EM maps of
1005 Cx46/50 channels under varying conditions, illustrating lipid-mediated and reversible pH gating. NT
1006 domains in open and gated-states are shown in dark blue and light blue, respectively, with lipids in
1007 orange. Specimens from different preparations are separated by vertical dashed lines. **a** Cx46/50
1008 reconstituted in amphipol (PMAL-C8) at low pH, showing the NT in the open-state with no lipid (or
1009 detergent) densities observed in the pore. **b** Cx46/50 reconstituted into nanodiscs (containing DMPC
1010 lipids) and maintained in neutral pH conditions, showing the open-state with the pore free of lipids. **c** The
1011 same sample after exchange to low pH, resulting in the gated-stated with pore bound lipids (inset,
1012 highlights lipid densities). **d** Cx46/50 reconstituted into nanodiscs at neutral pH, then exchanged to pH
1013 5.8 and maintained at low pH, showing the gated-state with pore-bound lipids (inset). **e** The same low
1014 pH sample returned to neutral pH resulting in the open-state and the pore is devoid of lipids.

1015

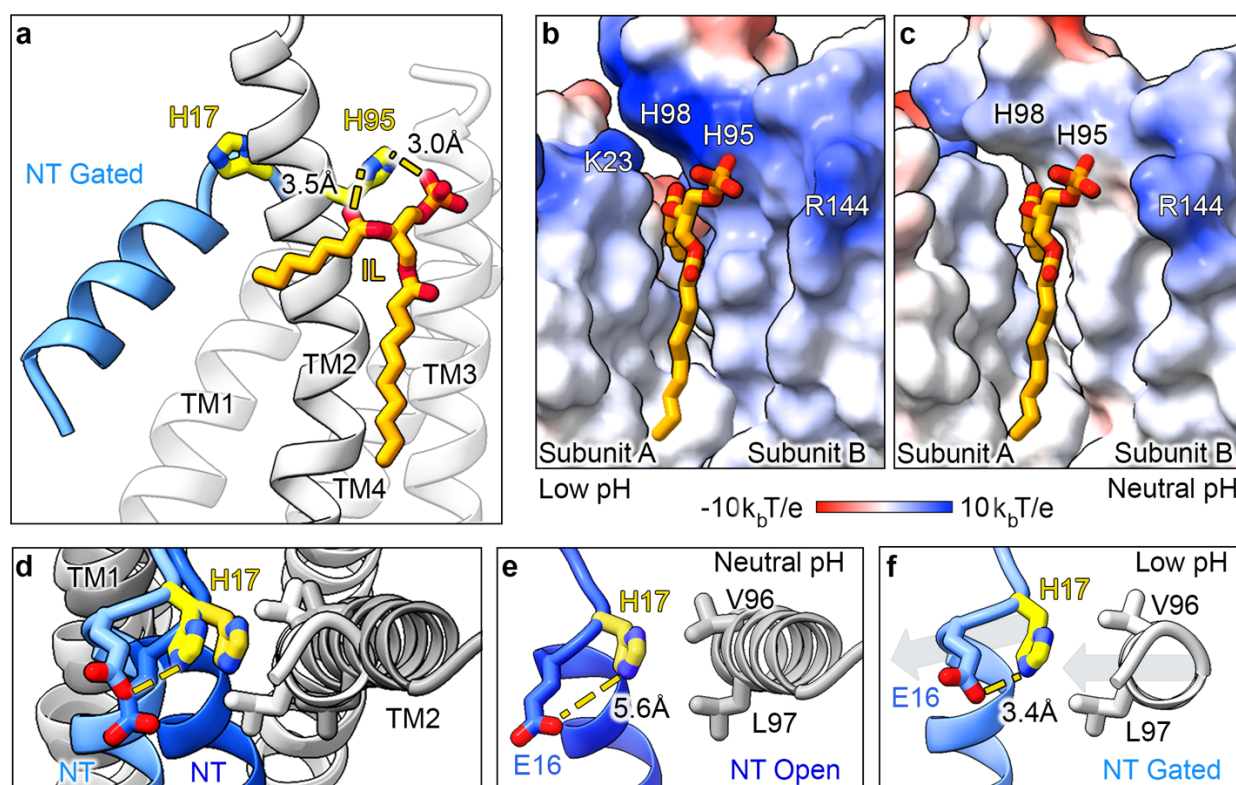1016

30

1017   **Figure 4**

1018

1019   **Figure 4. Putative roles of conserved histidine residues in pH-gating. a** Zoomed view of a Cx46/50

1020   subunit highlighting conserved histidine residues (yellow, stick representation): H17 on the NT (light blue)

1021   and H95 on TM2, oriented toward the lipid bilayer. The imidazole ring of H95 is within 3.0–3.5 Å of the

1022   negatively charged phosphate group and glycerol backbone of the interstitial lipid (IL; shown in orange,

1023   stick representation). **b** Zoomed view of the IL (orange, stick representation) intercalated at the Cx46/50

1024   subunit interface (surface representation) colored by Coulombic potential (red – negative; white – neutral;

1025   blue - positive). The IL phosphate headgroup is accommodated by a positively charged cluster of

1026   positively charged amino acids, including the protonated states of H95 and H98, as well as K23 (R23 in

1027   Cx50) and R144 (R156 in Cx50). **c** The same IL binding site displayed with non-protonated states of H95

1028   and H98. **d** Cytoplasmic view comparing the stabilized open-state (7JKC, NT – dark blue; TMs – gray)

1029   and gated-state (NT – light blue; TMs – white), showing correlated movements of the NT and TM2

1030   involving rearrangements of E16 and H17. **e** At neutral pH, the imidazole ring of H17 is 5.6 Å from

1031   carboxylate sidechain of E16 and forms van der Waals interactions with V96 and L97 (A96 and V97 in

1032   Cx50) on TM2. **f** In the low pH gated-state, correlated movement of the NT and TM2 positions imidazole

1033   ring of H17 within salt-bridge distance (3.4 Å) of the negatively charged E16 sidechain. Panels b-f display

1034   models of Cx46 as the representative isoform.

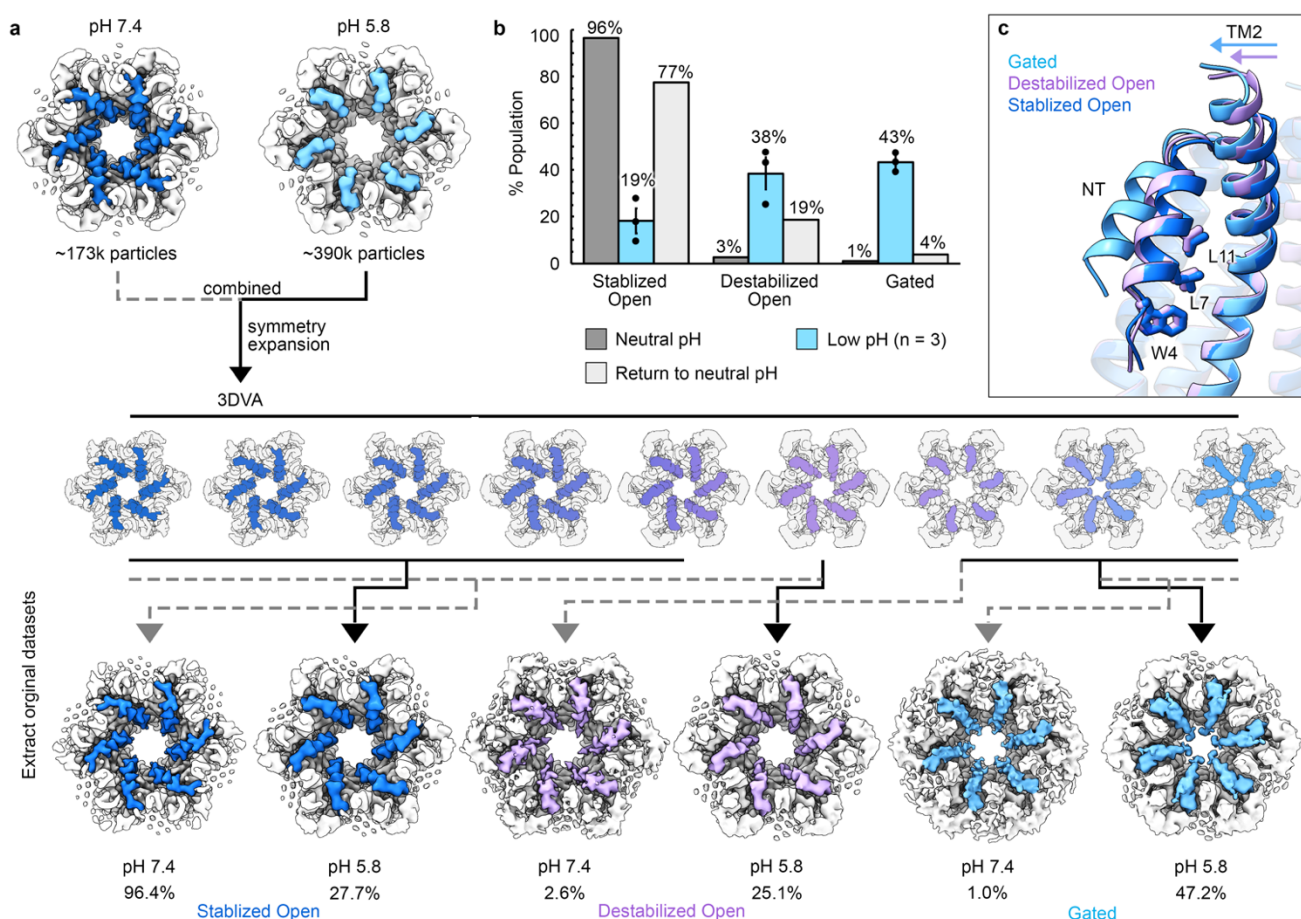1035

31

1036   **Figure 5**

1037

1038   **Figure 5. Low pH shifts the equilibrium ensemble of gated- and open-states. a** Flow diagram
1039   summarizing the image processing strategy used to classify three distinct states of Cx46/50: stabilized
1040   open-state (NT – dark blue), destabilized open-state (NT – pink), and gated-state (NT – light blue),
1041   identified under neutral and low pH conditions. **b** Bar chart showing percent populations of the three
1042   states at neutral pH (gray, n = 1), after exchange to low pH (light blue, n = 3; mean ± s.e.m.), and after
1043   return to neutral pH following low pH exposure (light gray, n = 1). Low pH shifts the conformational
1044   equilibrium predominantly toward the gated-state. **c** Structural overlay of the three states, highlighting
1045   primary conformational differences localized to the NT and TM2 domains. The NT of the destabilized
1046   open-state shows slight displacement relative to the stabilized open-state, accompanied by a ~6.4°
1047   movement of TM2 stemming from the P88 kink.

1048

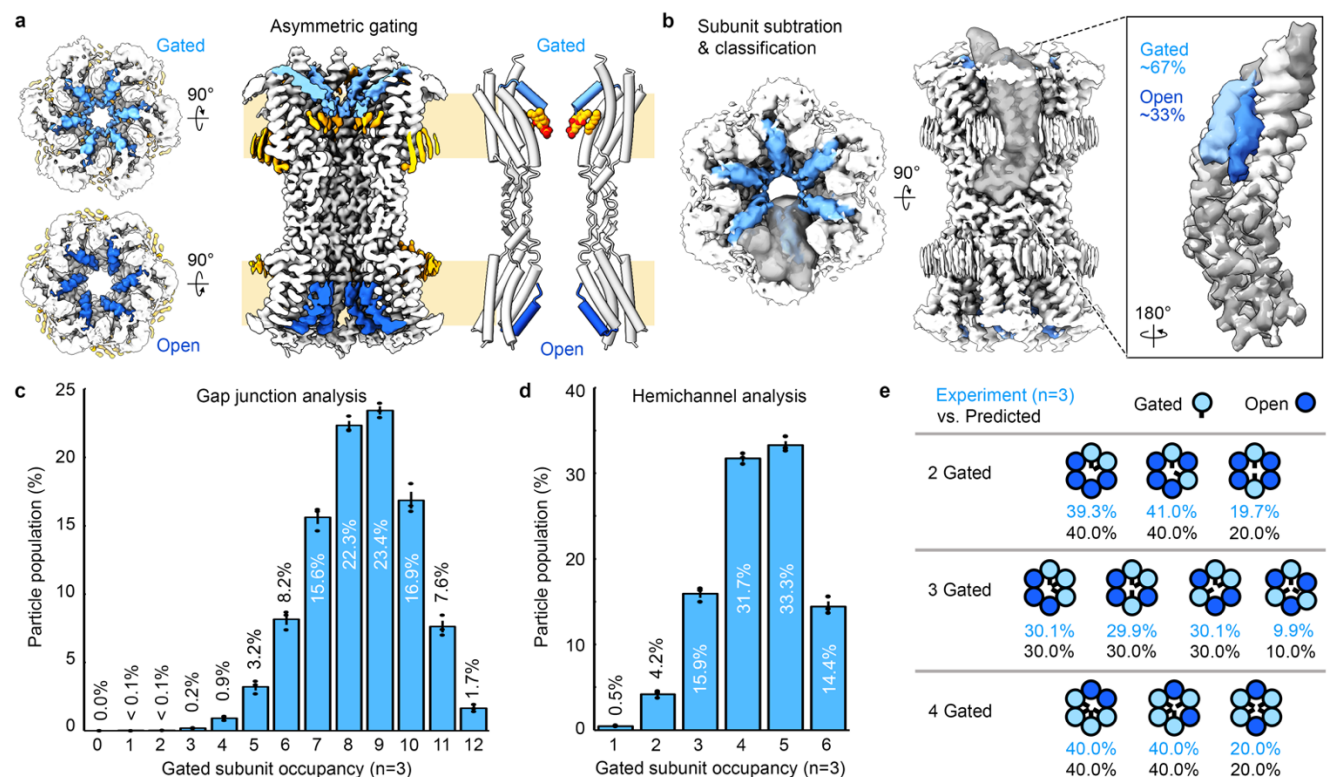1049

32

1050 **Figure 6**

1051

1052 **Figure 6. NT gating of Cx46/50 at low pH is non-cooperative. a** Cryo-EM map and model of a an
1053 asymmetrically gated-state of the Cx46/50, where one side of the intercellular channel is gated (NT –
1054 light blue) with pore-bound lipids (orange), while the opposite side adopts the stabilized open-state. **b**
1055 Top and side views of the mask (grey) used for the symmetry expansion and signal-subtraction protocol,
1056 used to isolate density corresponding to the individual subunits for 3D classification. Inset, showing
1057 overlay of cryo-EM maps identified in the open-state (dark gray and dark blue NTs) and gated-state (light
1058 gray and light blue NTs) following signal-subtraction and 3D classification, where 67.0% ± 0.5% (mean ±
1059 s.e.m.; n = 3) were classified in the gated-state. **c** Bar chart showing the population of gated-state
1060 monomers identified at the gap junction level, and **d** hemichannel level. The populations display
1061 Boltzmann-like distributions, with the largest populations corresponding to nine gated subunits (23.4% ±
1062 0.3%) at the gap junction level (panel c) and five gated subunits (33.3% ± 0.5%) at the hemichannel level
1063 (panel d). Bar charts show mean ± s.e.m. (n = 3), with individual data points displayed (black dots). **e**
1064 Possible configurations of open (dark blue) and gated-states (light blue) with quasi-equivalent number of
1065 gated subunits within each hemichannel. Each configuration is annotated with experimentally determined
1066 populations (mean; n = 3) compared to values assuming random distribution. The close correspondence
1067 of these values indicates NT gating at the subunit level is non-cooperative.

1068

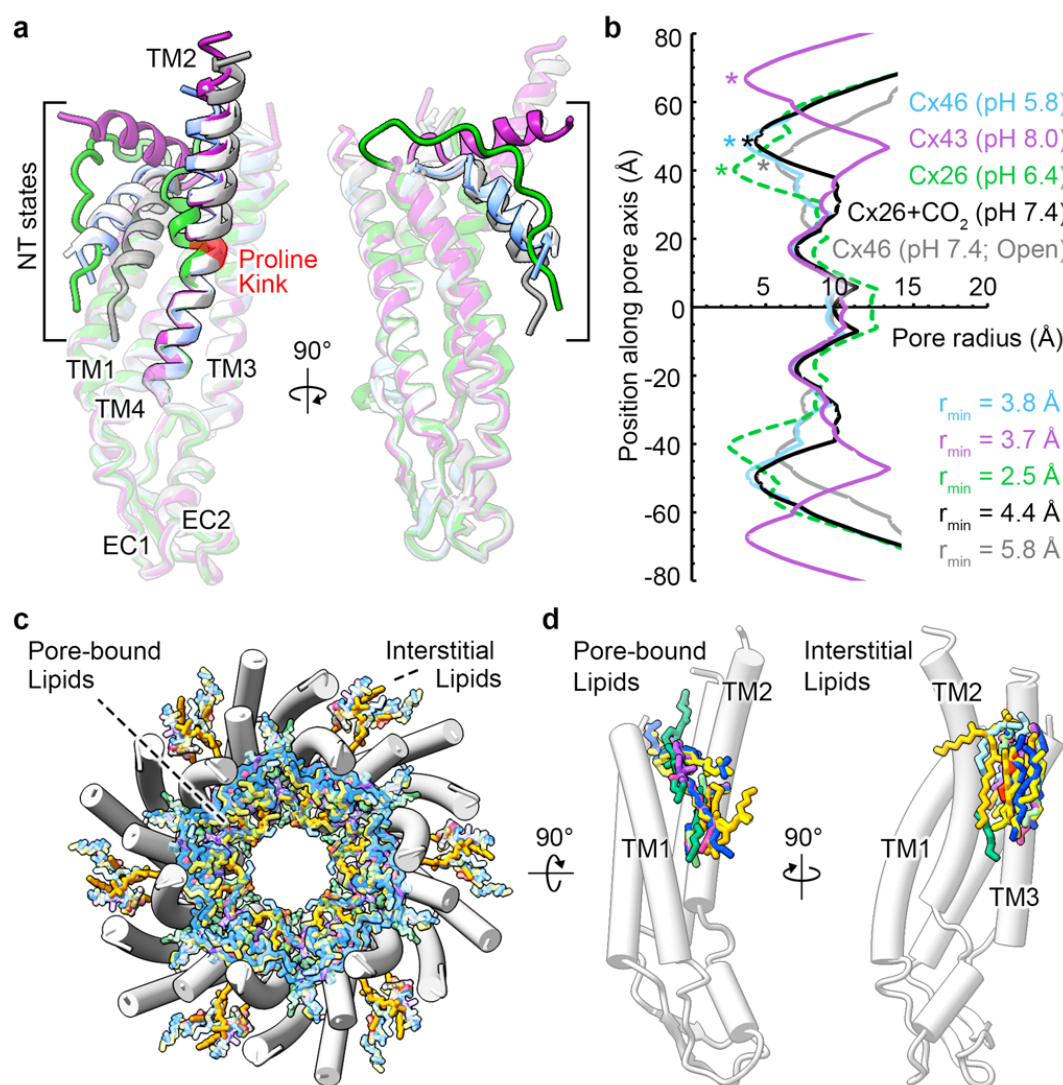1069

33

1070   **Figure 7**

1071

1072   **Figure 7. Structural comparison to connexin gap junctions under chemical-gating conditions. a**

1073   Structural overlay of connexin subunits: Cx46 at pH 7.4 (7JKC, open-state, gray), Cx46 at pH 5.8 (gated-

1074   state, light blue), Cx26 at pH 6.4 (6UVT, green), Cx26 treated with CO_2 maintained at pH 7.4 (7QEQ,

1075   white) and Cx43 at pH 8.0 (7F93, purple). The NT domain exhibits the most conformational variation,

1076   ranging from the stabilized open-state of Cx46 (pH 7.4), aligned along the pore axis, to the lifted NT

1077   conformation of Cx43, oriented orthogonal to the pore axis. The low pH gated-state NT of Cx46 (pH 5.8)

1078   most closely resembles the CO_2–treated Cx26 structure (Cα r.m.s.d. = 1.2 Å). TM2 shows differences

1079   stemming from a conserved proline kink (red). **b** Pore profile plot of the structures in panel a, colored

1080   accordingly. Asterisks indicate points of minimum radius (r_{min}) for the modeled regions. The plot for Cx26

1081   at low pH (6uvt, dotted line) reflects the absence of sidechains in the deposited model. **c** Top view of the

1082   Cx46 gap junction with the NT's hidden, and superposition of lipids modeled in the channel pore of Cx46

1083   at low pH (orange), Cx26 (7QEQ, red; 8QA0, grey), Cx36 (8IYG, green; 7XNH, light blue), and Cx43

1084   (7F92, pink; 7XQF, yellow; 7XQB, blue; 7F93, light green), all sharing a similar trend of occupying

1085   portions of the channel lumen and at subunit interfaces. **d** *Left,* Cx46 subunits (NT hidden), showing

34

1086   superimposed pore-bound lipids (stick representation) from various connexin structures: Cx46 at low pH

1087   (orange), Cx36 (7XKT, green; 8IYG, purple), and Cx43 (7F92, pink; 7XQF yellow; 7XQB, blue; 7F93,

1088   green). *Right,* Cx46 subunit (NT hidden), showing superimposed annular lipids near the IL site from

1089   various connexin structures: Cx46 at low pH (orange), Cx26 treated with CO_2 (7QEQ, red), Cx36 (7XKT,

1090   green; 8IYG, purple; 7XNH, light blue), and Cx43 (7F92, pink; 7XQF, yellow; 7XQB, blue; 7F93, green).
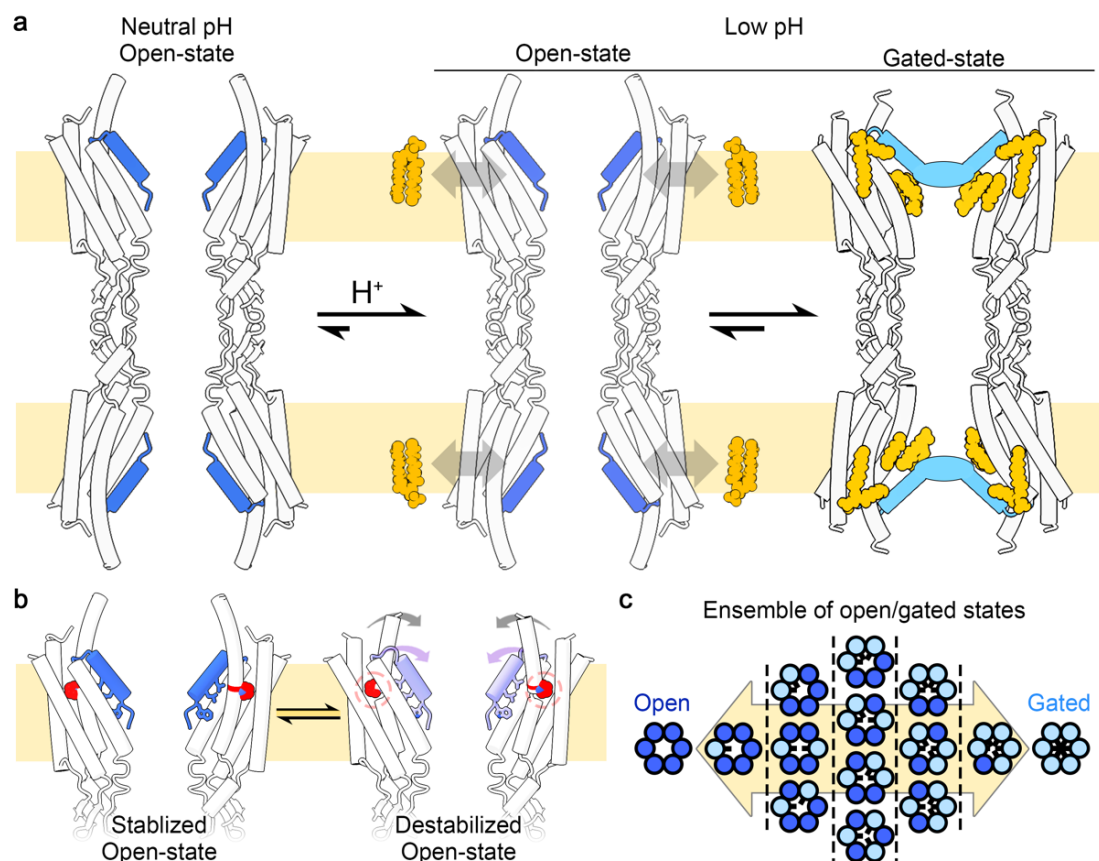
1091

1092 **Figure 8**

1093

1094 **Figure 8. Schematic of reversible lipid-mediated pH gating of Cx46/50. a** At neutral pH, Cx46/50 gap
1095 junctions predominantly adopt an open-state (NT – dark blue). At low pH, the equilibrium shifts toward
1096 an ensemble of open- and gated-states (NT – light blue), with the gated-state being most populated.
1097 Lipids (orange) translocate from the membrane environment into the pore, displacing the NT and
1098 occluding the channel permeation pathway. Upon returning to neutral pH, pore-bound lipids diffuse back
1099 to the membrane, and the NT returns to the open-state conformation. **b** The open-state represents a
1100 conformational equilibrium between a stabilized open-state and a less populated destabilized open-state
1101 (NT – pink), characterized by a slight displacement of the NT and bending of TM2 at a conserved proline
1102 kink (red). **c** The gated-state comprises a complex ensemble of micro-states, with NT domains of
1103 individual subunits adopting non-cooperative gated-state conformations.

1104

1105

1106

1107

EXTENDED DATA (TABLES, FIGURES AND LEGENDS)

Data Collection and Processing Information

	1	1	1	5	6	6	6	2
Collection:	1	1	1	5	6	6	6	2
Condition:	pH 5.8	pH 5.8	pH 5.8	pH 5.8	pH 7.4	pH 7.4	pH 7.4	pH 5.8
State:	Gated	Destabilized-Open	Stable-Open	Asymmetrically Gated	Gated	Destabilized-Open	Stable-Open	Stable-open
Magnification	29,000	29,000	29,000	105,000	105,000	105,000	105,000	105,000
Voltage (kV)	300	300	300	300	300	300	300	300
Electron Exposure (e-/Å^2)	50	50	50	50	50	50	50	50
Defocus Range (μm)	-0.8 to -2.2	-0.8 to -2.2	-0.8 to -2.2	-0.5 to -1.8	-0.5 to -1.8	-0.5 to -1.8	-0.5 to -1.8	-0.8 to -2.2
Pixel size (Å)	0.8015	0.8015	0.8015	0.8220	0.8220	0.8220	0.8220	0.665
Symmetry imposed	D6	D6	D6	C6	D6	D6	D6	D6
Initial particle images (no.)	2,503,619	2,503,619	2,503,619	6,838,630	4,002,015	4,002,015	4,002,015	502,309
Final particle images (no.)	190,184	218,088	42,656	162,334	15,342	75,136	311,313	127,102
Map resolution (Å)	2.2	2.2	2.5	2.4	2.7	2.2	2.0	2.7
FSC threshold	0.143	0.143	0.143	0.143	0.143	0.143	0.143	0.143
Map resolution range (Å)	1.9 – 4.5	1.9 – 4.5	2.1 – 5.5	1.8 – 5.5	2.5 – 6.7	1.8 – 5.5	1.8 – 4.0	1.4 – 9.3

Connexin-46: Refinement and validation statistics

	1	1	1	5	6	6	6	2
Collection:	1	1	1	5	6	6	6	2
Condition:	pH 5.8	pH 5.8	pH 5.8	pH 5.8	pH 7.4	pH 7.4	pH 7.4	pH 5.8
State:	Gated	Destabilized-Open	Stable-Open	Asymmetrically Gated	Gated	Destabilized-Open	Stable-Open	Stable-open
Initial model used (PDB code)	7JKC	7JKC	7JKC	7JKC	7JKC	7JKC	7JKC	7JKC
Model resolution (Å)	2.4	2.4	2.5	2.5	3.2	2.5	2.1	3.0
FSC threshold	0.5	0.5	0.5	0.5	0.5	0.5	0.5	0.5
Model resolution range (Å)	2.1 - 2.4	2.2 - 2.4	2.4 - 2.5	2.3 - 2.5	2.6 - 3.2	2.2 - 2.5	2.0 - 2.1	2.5 – 3.0
Map sharpening B-factor (Å^2)	6.48	93.24	101.26	90.94	103.04	86.94	73.02	129.36
Model composition								
Non-hydrogen atoms	51,060	45,468	42,372	44,742	43,608	45,552	48,504	35,592
Protein residues	2220	2244	2196	2208	2220	2244	2280	2184
Ligands	420	288	180	246	228	276	312	0
B factors (Å^2)								
Protein	6.48	93.24	101.26	90.94	103.04	86.94	73.02	129.36
Ligand	12.67	111.45	114.72	112.22	27.29	104.67	103.67	-
R.M.S. deviations								
Bond lengths (Å)	0.006	0.004	0.004	0.005	0.004	0.004	0.004	0.007
Bond angles (º)	1.587	1.103	1.088	1.365	1.084	1.121	1.251	1.178
Validation								
MolProbity score	0.96	0.89	1.14	1.12	1.08	0.87	1.14	1.30
Clashscore	1.97	1.49	3.47	3.24	2.89	1.36	3.49	5.61
Poor rotamers (%)	0.00	0.60	0.57	0.61	0.61	0.60	0.59	0.62
Ramachandran plot								
Favored (%)	98.90	98.36	98.32	98.33	99.45	98.91	98.39	98.31
Allowed (%)	1.10	1.64	1.68	1.67	0.55	1.09	1.61	1.69
Disallowed (%)	0.00	0.00	0.00	0.00	0.00	0.00	0.00	0.00

Connexin-50: Refinement and validation statistics

	1	1	1	5	6	6	6	2
Collection:	1	1	1	5	6	6	6	2
Condition:	pH 5.8	pH 5.8	pH 5.8	pH 5.8	pH 7.4	pH 7.4	pH 7.4	pH 5.8
State:	Gated	Destabilized-Open	Stable-Open	Asymmetrically Gated	Gated	Destabilized-Open	Stable-Open	Stable-open
Initial model used (PDB code)	7JKC	7JKC	7JJP	7JKC	7JKC	7JKC	7JJP	7JJP
Model resolution (Å)	2.4	2.4	2.5	2.5	3.1	2.5	2.1	2.9
FSC threshold	0.5	0.5	0.5	0.5	0.5	0.5	0.5	0.5
Model resolution range (Å)	2.1 - 2.4	2.2 - 2.4	2.4 - 2.5	2.3 - 2.5	2.6 - 3.1	2.2 - 2.5	2.0 - 2.1	2.5 - 2.9
Map sharpening B-factor (Å^2)	8.64	92.73	101.81	93.30	104.78	88.34	71.70	131.24
Model composition								
Non-hydrogen atoms	50,940	45,264	42,684	44,592	43,452	45,336	48,204	35,412
Protein residues	2220	2244	2220	2208	2220	2244	2280	2184
Ligands	420	288	180	246	228	276	312	0
B factors (Å^2)								
Protein	8.64	92.73	101.81	93.30	104.78	88.34	71.70	131.24
Ligand	12.67	111.45	112.75	112.22	90.39	103.02	101.48	-
R.M.S. deviations								
Bond lengths (Å)	0.005	0.004	0.004	0.005	0.004	0.008	0.006	0.003
Bond angles (º)	1.477	1.121	1.016	1.346	1.106	1.171	1.244	0.558
Validation								
MolProbity score	1.06	0.95	1.07	1.11	1.14	1.12	1.05	1.20
Clashscore	2.76	1.86	2.77	3.24	3.46	3.24	2.65	4.14
Poor rotamers (%)	0.00	0.00	0.60	0.60	0.59	0.59	0.57	0.60
Ramachandran plot								
Favored (%)	100.0	98.91	99.45	98.89	99.45	98.36	98.92	99.44
Allowed (%)	0.00	1.09	0.55	1.11	0.55	1.64	1.08	0.56
Disallowed (%)	0.00	0.00	0.00	0.00	0.00	0.00	0.00	0.00

Extended Table 1. Cryo-EM data collection, refinement, and validation statistics.

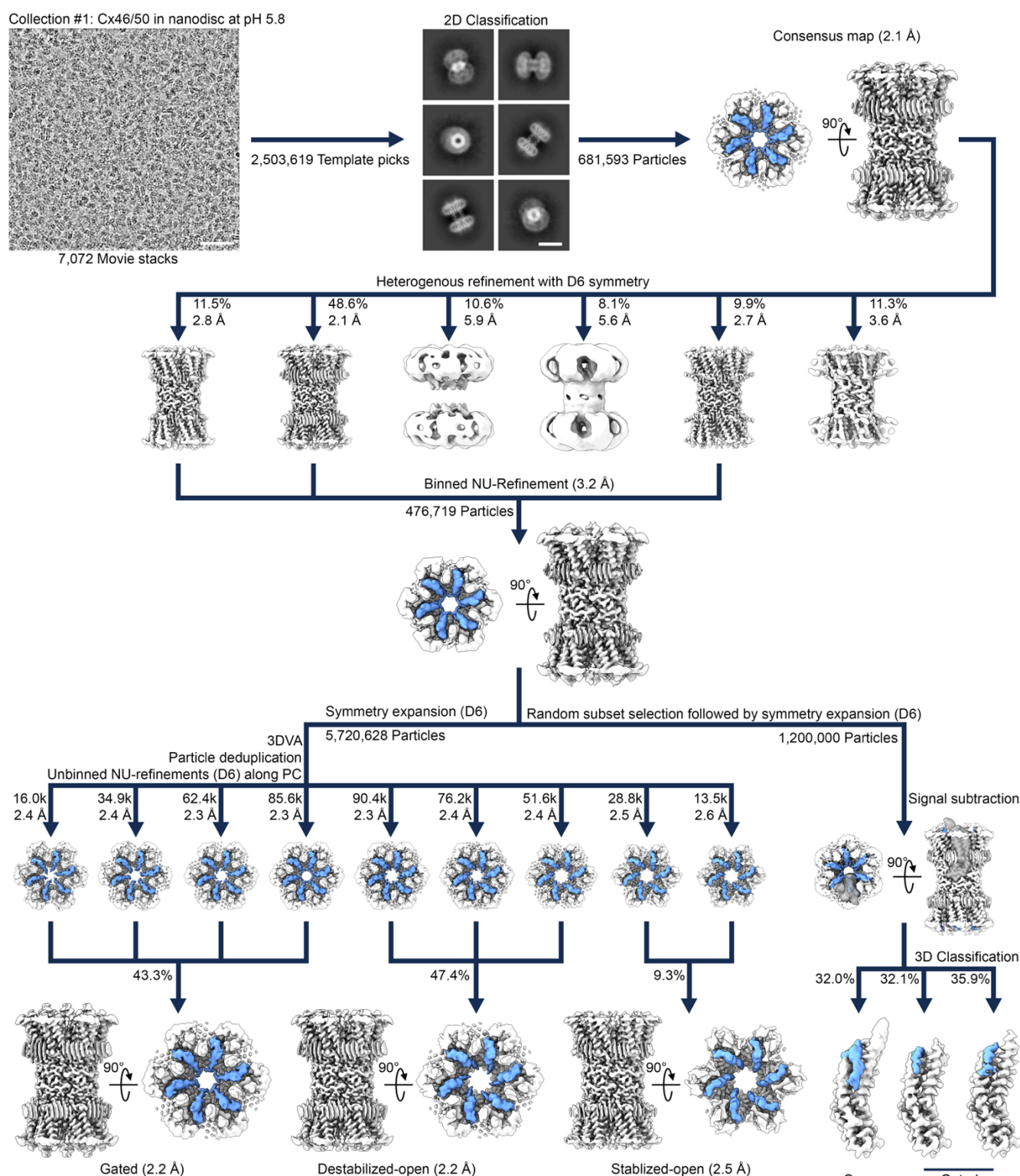1114 **Extended Data Figure 1**

1115
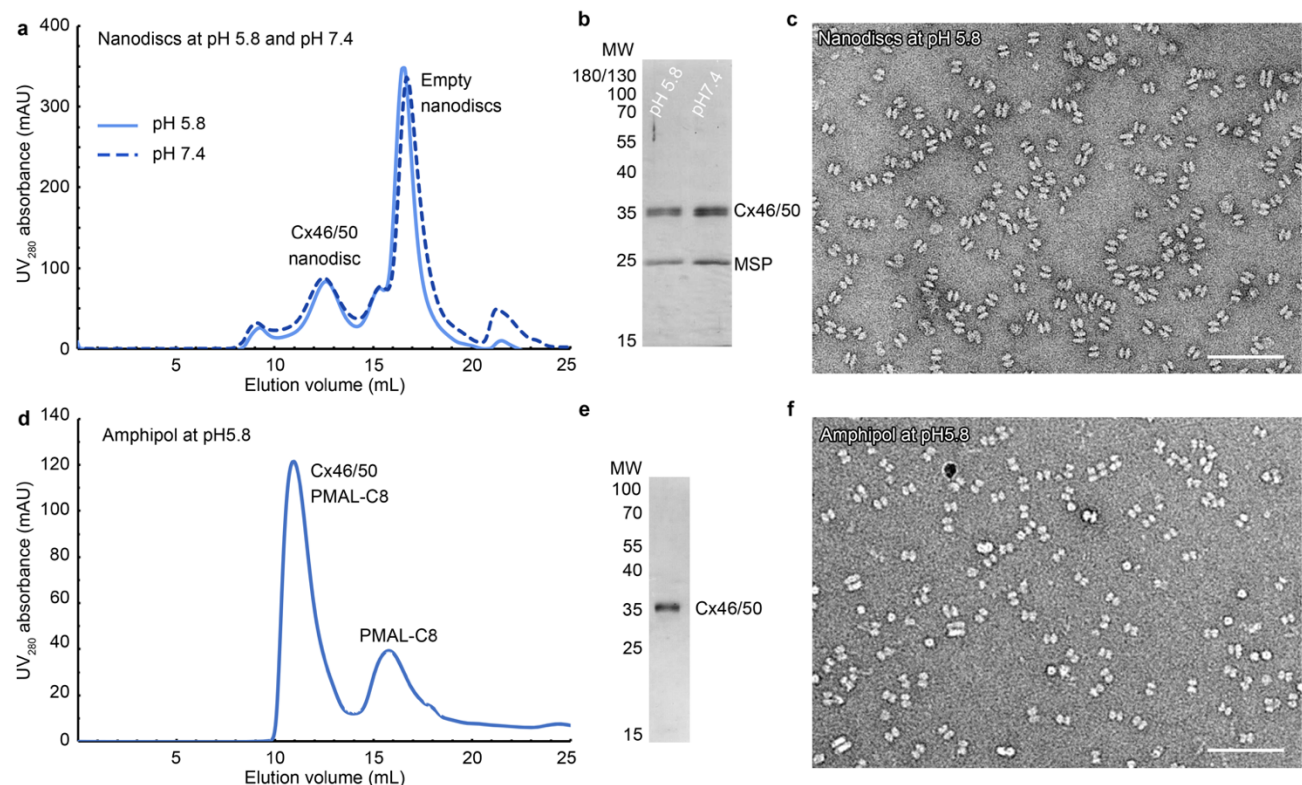
1116 **Extended Data Figure 1. Purification and reconstitution of connexin-46/50 in nanodiscs and**
1117 **amphipols. a** Gel filtration chromatography (Superose S6) traces monitored by UV absorbance at 280
1118 nm. Peaks containing native Cx46/50 gap junctions embedded in DMPC lipid nanodiscs (MSP1E1) and
1119 empty nanodiscs are labeled. Gel filtration traces at pH 5.8 (light blue) and pH 7.4 (dashed, dark blue)
1120 are nearly identical. **b** Silver stained SDS-PAGE of the gel filtration peak containing Cx46/50 embedded
1121 in nanodiscs, with molecular markers indicated. MSP1E1 migrates at ~24 kDa (predicted MW ~27.5 kDa),
1122 and native Cx46/50 gap junctions from the lens core migrate together as a band at ~38 kDa. **c** Electron
1123 micrograph of negatively stained particles from the pH 5.8 gel filtration fraction, containing Cx46/50 in
1124 nanodiscs (scale bar = 100 nm). Structures characteristic of Cx46/50 in nanodiscs are observed[41]. **d** Gel
1125 filtration chromatography (Bio-Rad ENrich SEC 650) trace monitored by UV absorbance at 280 nm.
1126 Peaks corresponding to native Cx46/50 reconstituted into amphipol (PMAL-C8) and PMAL-C8 micelles
1127 are labeled. **e** Silver stained SDS-PAGE of the gel filtration peak containing Cx46/50 in PMAL-C8 (band
1128 at ~38kDa), with molecular weight markers indicated. **f** Electron micrograph of negatively stained particles
1129 from the pH 5.8 gel filtration fraction, showing Cx46/50 in amphipol (scale bar = 100 nm). Particles appear
1130 identical to those previously reported for Cx46/50 in amphipol at pH 7.4[40].

1131

1132

1133 **Extended Data Figure 2**

1134
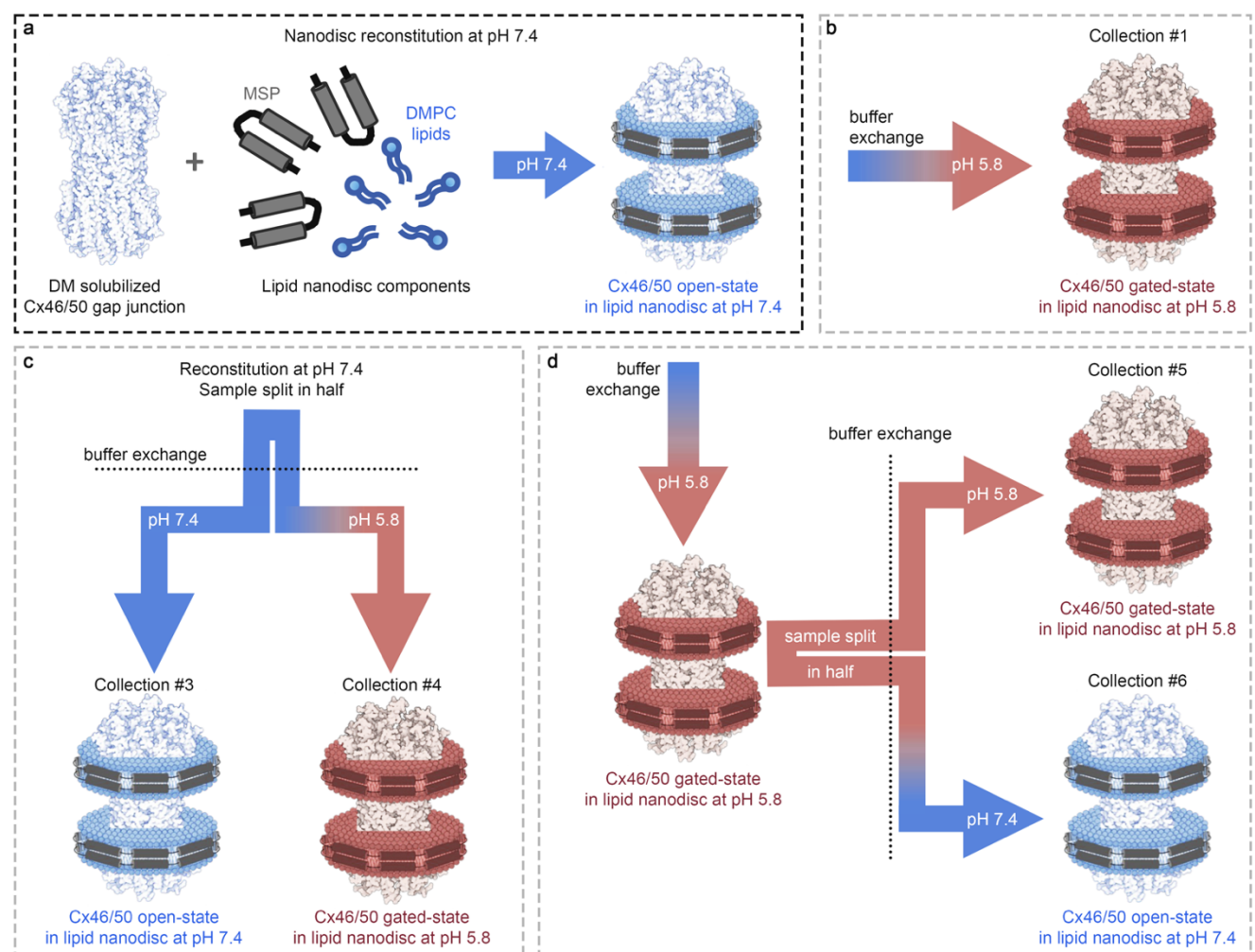
Extended Data Figure 2. Schematic of experimental design for pH- and lipid-dependent structural studies. a Native Cx46/50 gap junction channels were reconstituted into MSP1E1 nanodiscs containing DMPC lipids at pH 7.4. **b** For Collection #1, nanodisc-embedded Cx46/50 channels at pH 7.4 (panel a) were buffer exchanged by gel filtration to pH 5.8 and imaged by cryo-EM. **c** After reconstitution into nanodiscs at pH 7.4 (panel a), the sample was split in half and buffer exchanged by gel filtration to pH 7.4 (control, Collection #3) or pH 5.8 (Collection #4), followed by cryo-EM imaging. **d** Nanodisc-embedded Cx46/50 channels reconstituted at pH 7.4 were exchanged to pH 5.8 by gel filtration to induce gating. The sample was then split: one half was dialyzed into the same pH 5.8 buffer (control, Collection #5), while the other half was returned to pH 7.4 by dialysis (Collection #6). Both samples were then imaged by cryo-EM. Not shown: Cx46/50 gap junctions were reconstituted into amphipols at pH 7.4 and subsequently buffer exchanged to pH 5.8 by gel filtration (Collection #2).

1146

1147

1148

Extended Data Figure 3

Extended Data Figure 3. Cryo-EM image processing workflow for the low pH nanodisc dataset (Collection #1). Workflow for the low pH in nanodiscs containing DMPC lipids dataset (Collection #1). Representative cryo-EM micrograph (physical pixel size 0.802 Å^2; total dose ~50 e$^-$/Å^2) and 2D classes are shown with 50 nm and 10 nm scale bars, respectively. The dataset was processed using CryoSPARC, with representative maps shown at various stages of the pipeline. After blob picking and

40

1156   template generation (not shown), particles were selected using template picking followed by iterative 2D

1157   classification and particle deduplication. Particles underwent successive non-uniform (NU) refinements

1158   (D6 symmetry) and unbinning to yield a high-resolution consensus map. Heterogenous refinement (D6

1159   symmetry) was used to isolate high-resolution (< 3.0 Å) particles, which were subsequently binned (1.5

1160   Å pixel size) and subjected to NU-refinement (D6 symmetry). To assess particle heterogeneity at the

1161   subunit-level, signal subtraction was performed on a random subset of symmetry expanded (D6)

1162   particles, yielding 1.2M monomer particles for signal subtraction and 3D classification. 3D classification

1163   revealed primarily gated-state monomers, with a minor population of open-state monomers. To assess

1164   particle heterogeneity at the gap junction-level, particles were symmetry expanded (D6) and subjected

1165   to 3D variability analysis (3DVA). A mask generated to exclude the nanodisc was used. The primary

1166   principal component was divided into nine non-overlapping frames, each locally refined using D6

1167   symmetry. Particles were then deduplicated and subjected to NU-refinement (D6 symmetry). Particles

1168   yielding similar 3D reconstructions (classified as gated, destabilized open, and stabilized open-states

1169   based on conformation of the NT domain – blue) were pooled and subjected to a final round of NU-

1170   refinement with applied D6 symmetry.

1171

1172   **Extended Data Figure 4**

1173
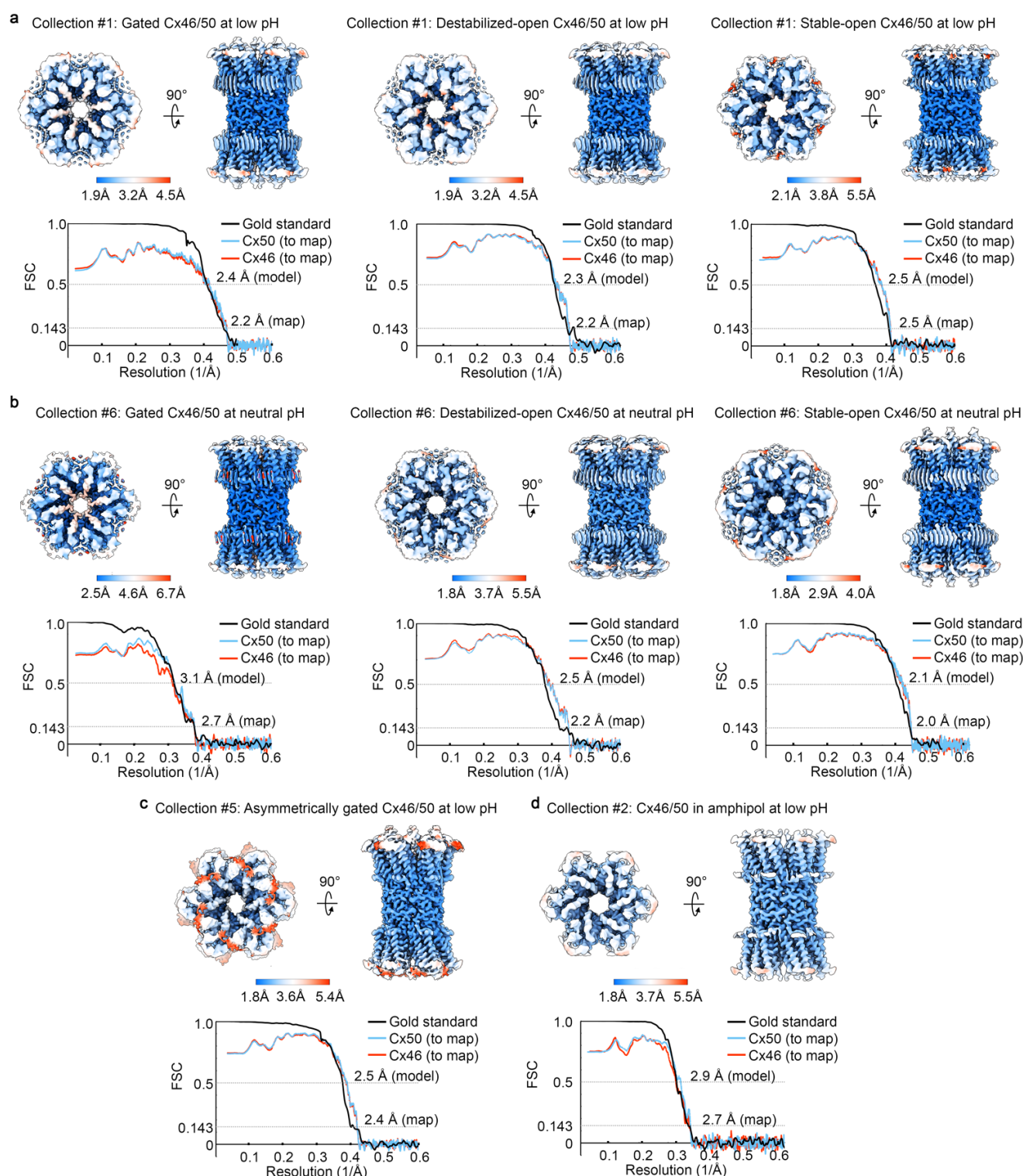
1174   **Extended Data Figure 4. Resolution assessment of cryo-EM 3D reconstructions.** Local resolution

1175   analysis of final cryo-EM 3D reconstructions using CryoSPARC, displayed by colored surface. Fourier

1176   Shell Correlation (FSC) analysis obtained from final 3D reconstructions. Gold-Standard FSC (black)

1177   indicating global resolutions (0.143 cut-off). FSC curves comparing atomic models for Cx46 (red) and

1178   Cx50 (blue) fit to the respective final cryo-EM 3D reconstruction (0.5 cut-off). Resolution assessment is

1179   shown for: **a** (Collection #1) *Left,* gated-state; *middle,* destabilized open-state; *right,* stabilized open-state

1180 obtained at low pH. **b** (Collection #6) *Left,* gated-state; *middle,* destabilized open-state; *right,* stabilized

1181 open-state obtained at neutral pH. **c** (Collection #5) Representative asymmetrically gated-state obtained

1182 at low pH. **d** (Collection #2) Stabilized open-state obtained at low pH in amphipol.

1183

1184

1185   **Extended Data Figure 5**
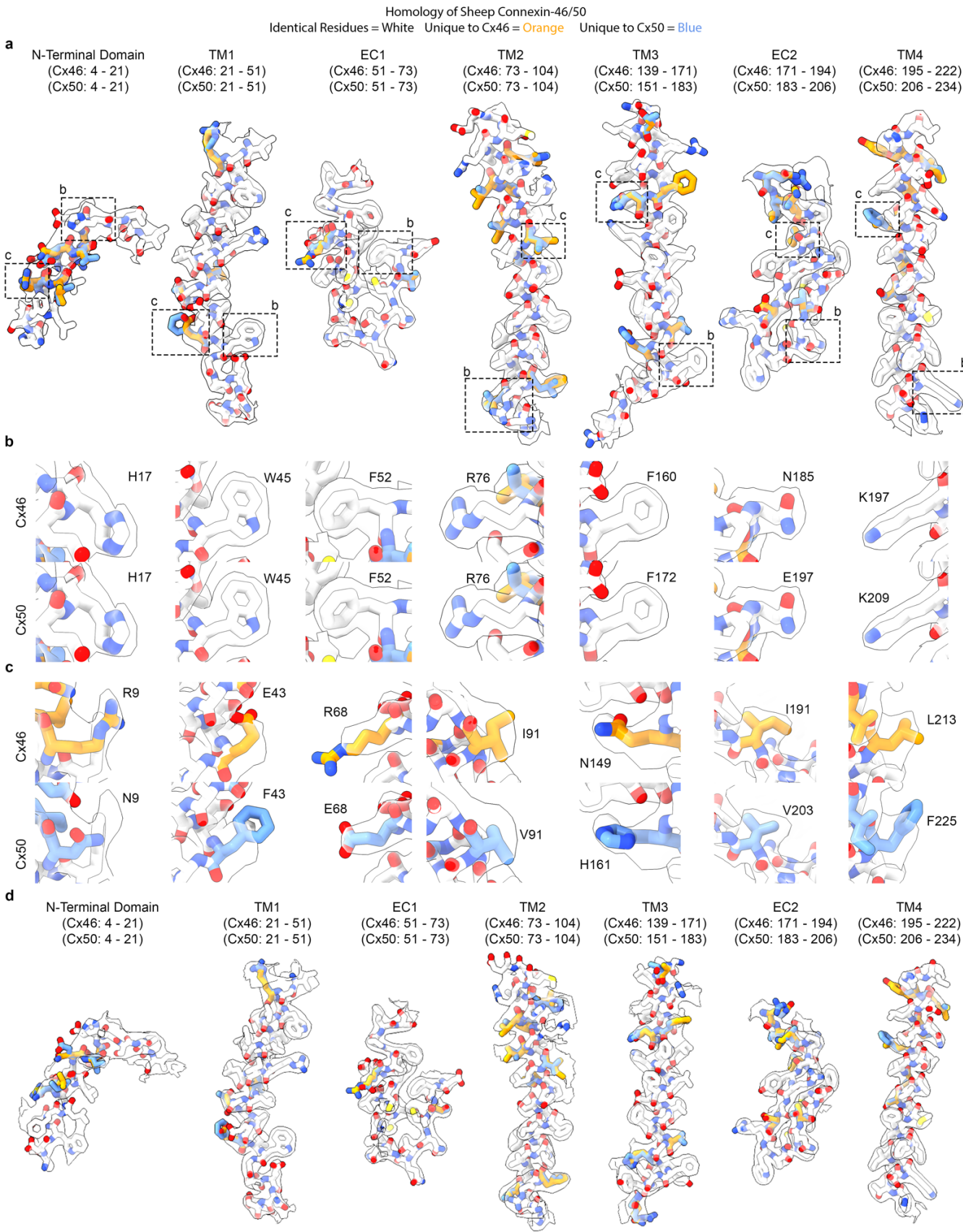
1186

1187   **Extended Data Figure 5. Fit of atomic models to the cryo-EM density map of the low pH gated-**

1188   **state. a** Segmented cryo-EM map for the low pH gated-state with atomic models for sheep connexin-46

1189   (Cx46) and connexin-50 (Cx50) fit to the experimental densities derived from Collection #1 (2.2 Å, D6-

1190   symmetry), including regions for the N-terminal domain, transmembrane domains 1-4 (TM1-4) and

1191   extracellular domains 1-2 (EC1-2). Cx46 and Cx50 models are colored according to their pair-wise

1192   sequence homology, as being identical (white), or unique (orange for Cx46; blue for Cx50). **b,c** Windows

1193   show zoom-views corresponding to boxed regions of the segmented maps, highlighting representative

1194   sidechain densities and fit to the atomic models. Regions of identical amino acids (panel b) are fit equally

1195   well by both models, whereas regions where the sequence of Cx46 and Cx50 differ (panel c), sidechain

1196   density is typically weaker or show features due to imposed averaging of two different sidechains in these

1197   areas (or relative flexibility of solvent exposed sidechains). **d** Segmented cryo-EM map for the low pH

1198   destabilized open-state with atomic models for sheep Cx46 and Cx50 fit to the experimental densities

1199   derived from Collection #1 (2.2 Å, D6-symmetry), including regions for the N-terminal domain, TM1-4,

1200   and EC1-2, colored as in panel a.

1201

1202

1203

1204

Extended Data Figure 6
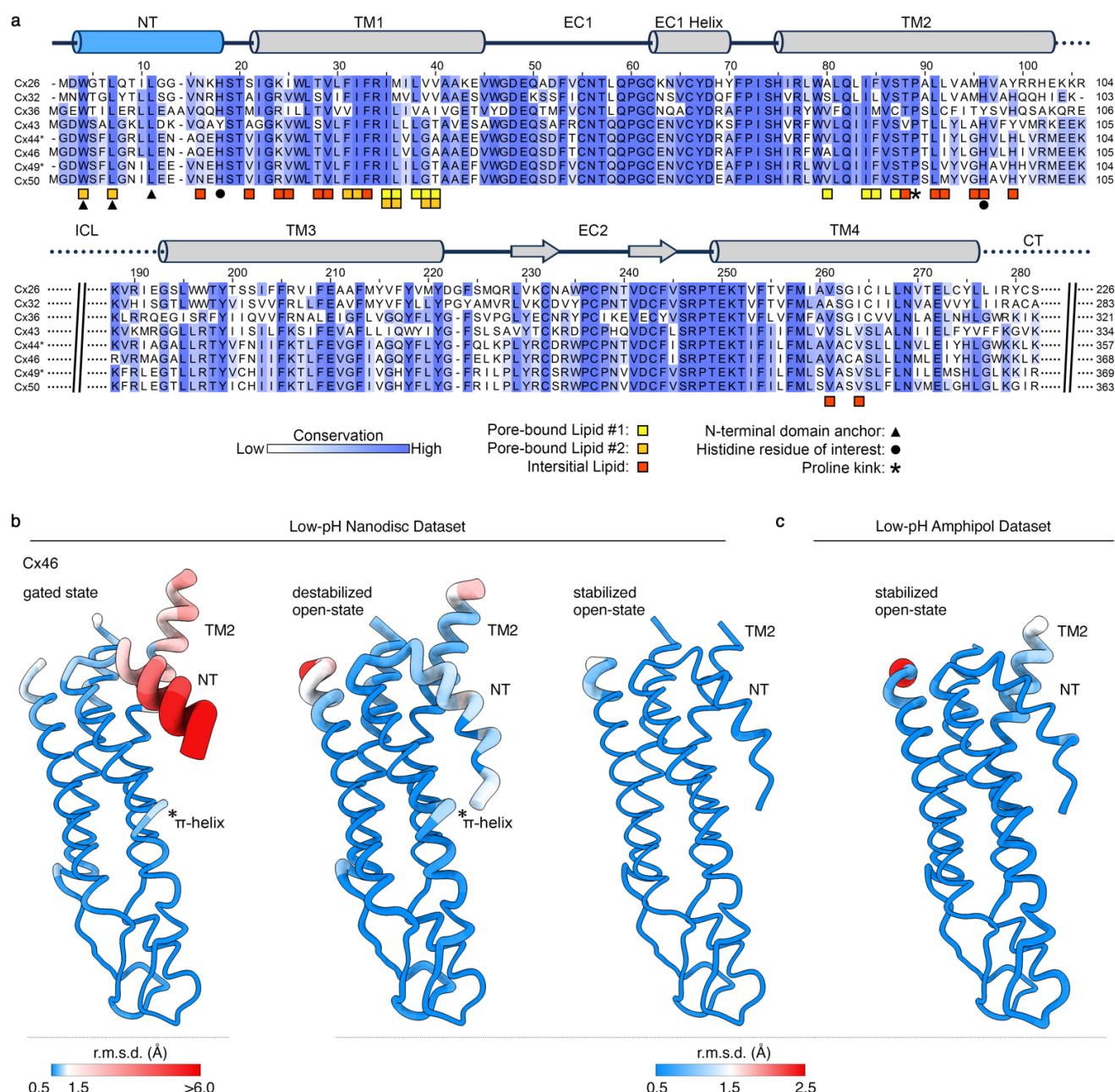
Extended Data Figure 6. Annotated sequence and structural alignments. a Sequence alignment and secondary structure topology of representative human and ovine (Cx44 and Cx49) connexin isoforms, colored by conservation. Conserved hydrophobic residues involved in N-terminal domain anchoring of the stabilized open-state of Cx46/50 are marked with triangles. Conserved histidine residues highlighted in this study (H17 and H95, Cx46/50 numbering) are indicated with circles. The conserved proline kink on TM2 is marked with an asterisk. Residues interacting with pore-bound lipids (PL1 and PL2) are annotated with yellow and orange squares, respectively. Residues interacting with the interstitial lipid (IL) are marked with red squares. **b** Structural alignment and Cα root mean square deviation (r.m.s.d.) analysis of Cx46 in a lipid nanodisc environment obtained in the low pH gated (left) destabilized open (center) and stabilized open (right) states versus the stabilized open state obtained at neutral pH (7JKC).

1217   **c** Structural alignment and Cα r.m.s.d. analysis of Cx46 in an amphipol environment obtained at low pH

1218   versus the stabilized open state obtained at neutral pH (7JKC). For panels b and c, r.m.s.d. values are

1219   visualized by color gradient (blue to red, indicating low to high values) and by the thickness of the

1220   backbone in 'worm' representation produced in ChimeraX. NT and TM2 domains are labeled. A key for

1221   r.m.s.d. values for each set of comparisons is displayed. Asterisk indicates region of minor variability

1222   around a π-helix that forms a kink in TM1 (residues ~39-41) observed in the gated and destabilized open-

1223   states.

1224

1225

1226   **Extended Data Figure 7**

1227
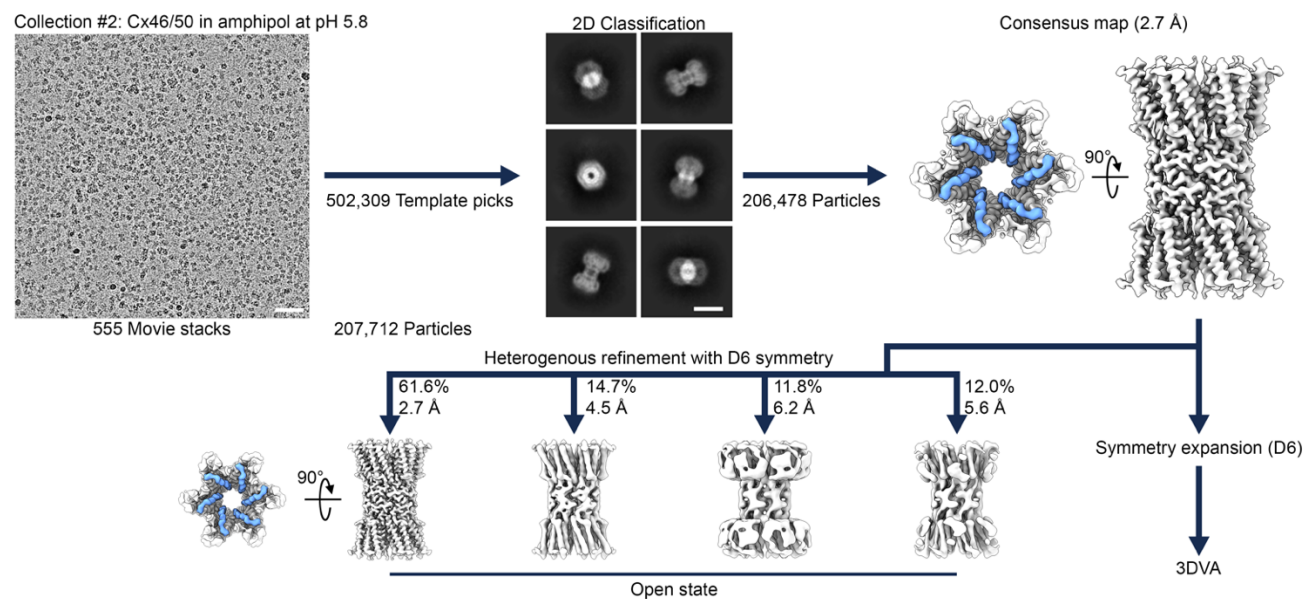
1228   **Extended Data Figure 7. Cryo-EM image processing workflow for the low pH amphipol dataset**
1229   **(Collection #2).** Workflow for the low pH in amphipol dataset (Collection #2). Representative cryo-EM
1230   micrograph (physical pixel size 0.665 $Å^2$; total dose ~80 $e^-/Å^2$) and 2D classes are shown with 50 nm and
1231   10 nm scale bars, respectively. The dataset was processed using CryoSPARC, with representative maps
1232   shown at various stages of the pipeline. After blob picking and template generation (not shown), particles
1233   were selected using template picking followed by iterative 2D classification and particle deduplication.
1234   Particles underwent successive non-uniform (NU) refinements (D6 symmetry) and unbinning to yield a
1235   high-resolution consensus map. Heterogenous refinement (D6 symmetry) was used to isolate high-
1236   resolution (< 3.0 Å) particles. This resulted in one class representing the stable-open state. To assess
1237   particle heterogeneity at the gap junction-level, particles from the consensus 3D reconstruction were
1238   symmetry expanded (D6) and subjected to 3D variability analysis (3DVA). A mask generated to exclude
1239   the detergent micelle was used.

1240

1241

1242

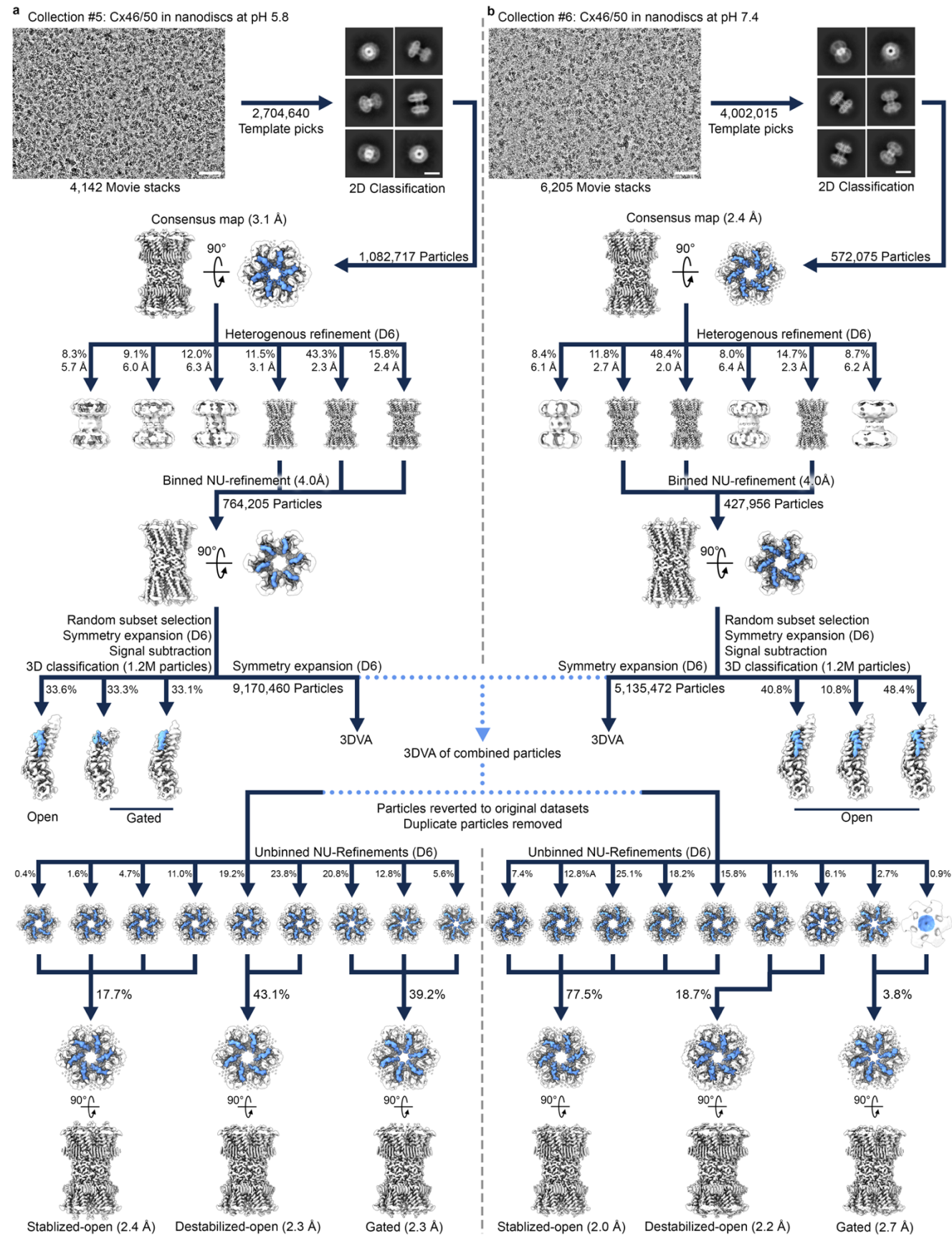1243

1244

1245

1246

1247

1248

48

1249 **Extended Data Figure 8**
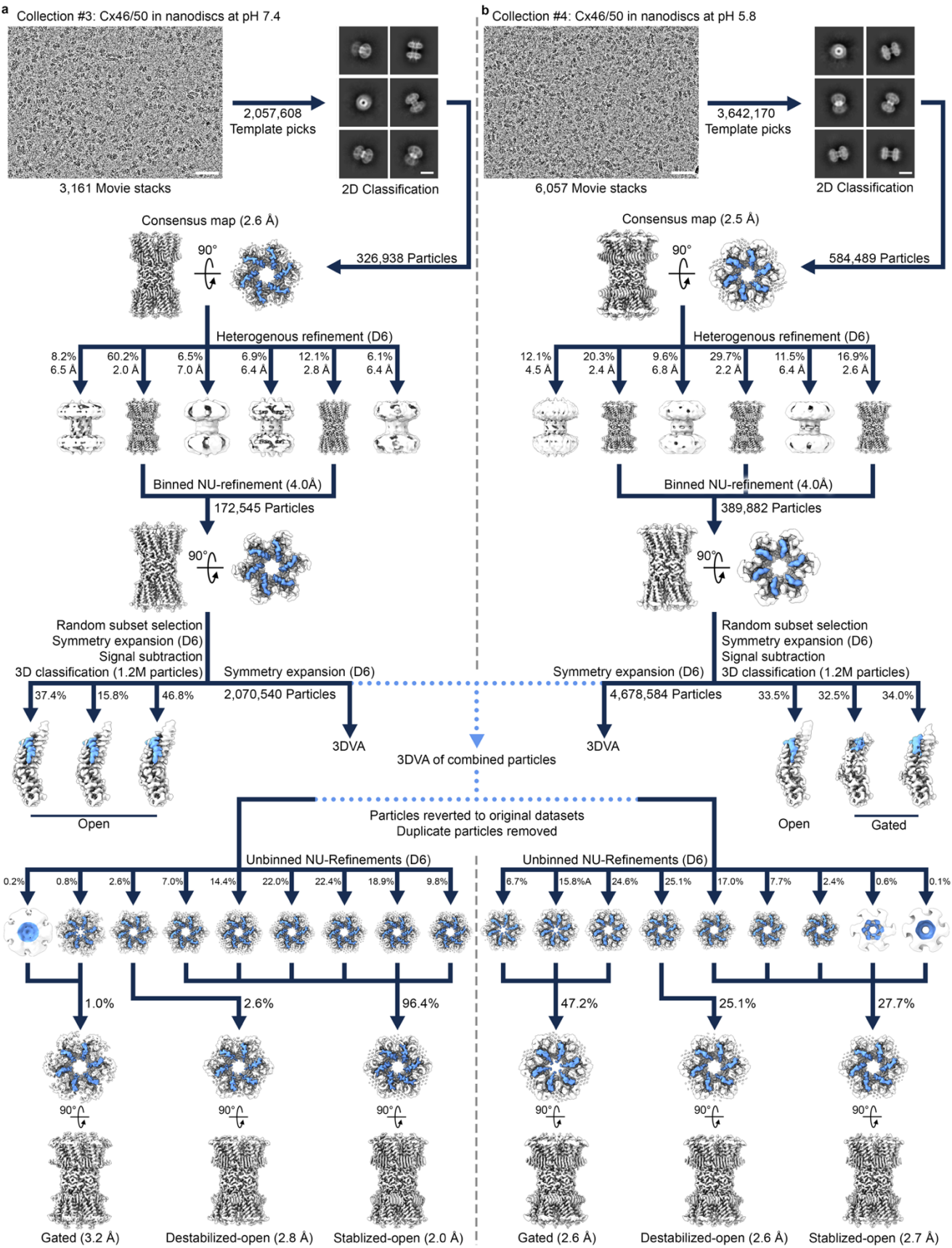
1250

1251 **Extended Data Figure 8. Cryo-EM image processing workflows for the split neutral (Collection #3)**

1252 **and low pH (Collection #4) datasets. a** Workflow for the neutral pH dataset (Collection #3).

49

Representative cryo-EM micrograph (physical pixel size 0.788 Å²; total dose ~50 e⁻/Å²) and 2D classes are shown with 50 nm and 10 nm scale bars, respectively. **b** Workflow for the low pH dataset (Collection #4), following the same general procedure as the neutral pH dataset. Representative cryo-EM micrographs and 2D classes are shown at equivalent scale. Both datasets were processed using CryoSPARC, with representative maps shown at various stages of the pipeline. After blob picking, and template generation (not shown), particles were selected using template picking followed by iterative 2D classification and particle deduplication. Particles underwent successive non-uniform (NU) refinements (D6 symmetry) and unbinning to yield a high-resolution consensus map. Heterogenous refinement (D6 symmetry) was used to isolate high-resolution (< 3.0 Å) particles, which were subsequently binned (2.0 Å pixel size) and subjected to NU-refinement (D6 symmetry). To assess particle heterogeneity at the subunit-level, signal subtraction was performed on a random subset of symmetry expanded (D6) particles, yielding 1.2M monomer particles for signal subtraction and 3D classification. For the neutral pH dataset (Collection #3), 3D classification only revealed open-state monomers. For the low pH dataset (Collection #4), 3D classification revealed primarily gated-state monomers, with a minor population of open-state monomers. To assess particle heterogeneity at the gap junction-level, particles were symmetry expanded (D6) and subjected to 3D variability analysis (3DVA). A mask generated to exclude the nanodisc was used for both datasets independently and on the combined datasets. The primary principal component for the combined datasets was divided into nine non-overlapping frames, each locally refined using D6 symmetry. Particles were then reverted to their original datasets, deduplicated, and subjected to NU-refinement (D6 symmetry). Particles yielding similar 3D reconstructions (classified as gated, destabilized open, and stabilized open-states based on conformation of the NT domain – blue) were pooled and subjected to a final round of NU-refinement with applied D6 symmetry.

1290 **Extended Data Figure 9**

1291 Stablized-open (2.4 Å) Destabilized-open (2.3 Å) Gated (2.3 Å) Stablized-open (2.0 Å) Destabilized-open (2.2 Å) Gated (2.7 Å)

1292 **Extended Data Figure 9. Cryo-EM image processing workflow for the reversibility of lipid-**
1293 **mediated pH gating low pH (Collection #5) and neutral pH (Collection #6) datasets. a** Workflow for

51

1294   the low pH dataset (Collection #5). Representative cryo-EM micrograph (physical pixel size 0.822 Å^2;

1295   total dose ~50 e$^-$/Å^2) and 2D classes are shown with 50 nm and 10 nm scale bars, respectively. **b**

1296   Workflow for the neutral pH dataset (Collection #6), following the same general workflow as the low pH

1297   dataset. Both datasets were processed using CryoSPARC, with representative maps shown at various

1298   stages of the pipeline. After blob picking and template generation (not shown), particles were selected

1299   using template picking followed by iterative 2D classification and particle deduplication. Particles

1300   underwent successive non-uniform (NU) refinements (D6 symmetry) and unbinning to yield a high-

1301   resolution consensus map. Heterogenous refinement (D6 symmetry) was used to isolate high-resolution

1302   (< 3.0 Å) particles, which were subsequently binned (2.0 Å pixel size) and subjected to NU-refinement

1303   (D6 symmetry). To assess particle heterogeneity at the subunit-level, signal subtraction was performed

1304   on a random subset of symmetry expanded (D6) particles, yielding 1.2M monomer particles for signal

1305   subtraction and 3D classification. For the neutral pH dataset (Collection #6), 3D classification only

1306   revealed open-state monomers. For the low pH dataset (Collection #5), 3D classification revealed

1307   primarily gated-state monomers, with a minor population of open-state monomers. To assess particle

1308   heterogeneity at the gap junction-level, particles were symmetry expanded (D6) and subjected to 3D

1309   variability analysis (3DVA). A mask generated to exclude the nanodisc was used for both datasets

1310   independently and on the combined datasets. The primary principal component for the combined

1311   datasets was divided into nine non-overlapping frames, each locally refined using D6 symmetry. Particles

1312   were then reverted to their original datasets, deduplicated, and subjected to NU-refinement (D6

1313   symmetry). Particles yielding similar 3D reconstructions (classified as gated, destabilized open, and

1314   stabilized open-states based on conformation of the NT domain – blue) were pooled and subjected to a

1315   final round of NU-refinement with applied D6 symmetry.

1316

1317

1318

1319 **SUPPLEMENTAL MOVIE LEGENDS**

1320

1321 o **Supplemental Movie 1: 3D variability analysis of Cx46/50 under varying pH and lipid**

1322 **conditions.**

1323 o **Supplemental Movie 2: Morph of Cx46/50 models illustrating the lipid-mediated pH gating**

1324 **mechanism.**

1325

1326

1327

1328

1329